PNAS
www.pnas.org

Supplementary Information for

Structural cavities are critical to balancing stability and activity of a membrane-integral enzyme

Ruiqiong Guo[a], Zixuan Cang[b], Jiaqi Yao[a], Miyeon Kim[a], Erin Deans[c,1], Guowei Wei[b], Seung-gu Kang[d,2], and Heedeok Hong[a,c,2]

[a]Department of Chemistry, Michigan State University, East Lansing, MI 48824; [b]Department of Mathematics, Michigan State University, East Lansing, MI 48824; [c]Department of Biochemistry & Molecular Biology, Michigan State University, East Lansing, MI 48824; [d]Computational Biology Center, IBM Thomas J. Watson Research Center, Yorktown Heights, NY 10598

[1]**Present address:** Graduate Program in Biochemistry and Biophysics, Brandeis University, Waltham, MA 02453.

[2]**To whom correspondence may be addressed.**
Email: sgkang@us.ibm.com or honghd@msu.edu

This PDF file includes:

Supplementary text
Figures S1 to S23
Tables S1 to S5
SI References

www.pnas.org/cgi/doi/10.1073/pnas.1917770117

Materials and Methods

Homology Modeling of Human Rhomboid Protease RHBDL2. The sequence alignment of human RHBDL2 (residues 71–266 spanning TM1–TM6 with TM7 truncated) and *Escherichia coli* GlpG on the basis of the predicted regions of transmembrane (TM) helices was obtained from Lemberg and Freeman (***SI Appendix,* Fig. S1A**) (1). The alignment and specified location of TM helices were passed to the Rosetta software suite (Rosetta3, build 2016.32.58837) for the comparative modeling of membrane proteins with multiple templates (2). Three *E. coli* GlpG structures (PDB codes: 2IC8 (3), 2XOV (4), and 3B45 (5)) were used as templates. The fragment library for the target was generated with the online Rosetta server (6). Ten models were constructed, among which three with the lowest energies were selected for further structural refinement using molecular dynamics (MD) simulations. In MD simulation, each model was embedded into a POPC (1-palmitoyl-2-oleoyl-phosphotadylcholine, $C_{16:0}C_{18:1c9}PC$) membrane (65Å x 65Å) constructed using the Membrane Builder module in VMD (Visual Molecular Dynamics, version 1.9.2) (7), followed by solvation in water. The artificial collisions were removed by deleting any lipid or water molecules that overlapped with the protein. The composite system was first relaxed for 10,000 steps of the conjugate gradient energy minimization, and further relaxed with a constrained MD in two stages: 0.5 ns with protein fixed and 0.5 ns with protein loosely restraint. Then a regular MD for 4 ns was run with no additional constraints for our refined models of human RHBDL2. All simulations were performed with NAMD2 software (8) and a protocol for membrane protein simulation (9) in the framework of CHARMM27 force field (10).

Identification of Common Cavities Among Three Rhomboid Proteases. GlpG of *E. coli* (PDB: 3B45) (5) and GlpG of *Haemophilus influenzae* (PDB: 2NR9) (11) were structurally aligned to Hs_RHBDL2 using the Matchmaker tool in the UCSF Chimera software (12). The RMSD for the 88 matched C_α pairs between 3B45 and Hs_RHBDL2 was 1.171 Å, and the RMSD for the 67 C_α pairs between 2NR9 and Hs_RHBDL2 was 1.056 Å. The superimposed as well as separate structures were submitted to the CASTp (Computed Atlas of the Surface Topography of proteins, http://sts.bioe.uic.edu/castp/index.html) server (13). To identify the cavities that are located in spatially common regions in the three rhomboid structures, we performed the cavity analysis directly on the superimposed structure using CASTp and the 1.0-Å-radius probe. The identified cavities would correspond to the free volumes common to all structures, or stem from the increased surface roughness upon superposition. The fictitious cavities in the latter were filtered out by mapping them back onto the structure of *E. coli* GlpG. If the heavy atoms surrounding a given cavity in *E. coli* GlpG shared at least one atom with those from a cavity in the superimposed structure, we defined the cavity surrounded by the shared atoms as “common”. This procedure was repeated for the cavities in *H. influenzae* GlpG and Hs_RHBDL2.

Molecular Dynamics Simulation of GlpG Wild Type (WT) and Variants. The cavity dynamics was investigated by all-atom molecular dynamics simulations for WT and variants with small-to-large mutations (*i.e.*, A142L, L143F, A164L, A182S, V203I, M208I, M249L, A250L, G252L, A256I, V260I, A164L/M208I, A164L/A250L, M208I/A250L). We first simulated for GlpG WT, and then moved on for each variant on the basis of the equilibrated WT conformation. The WT system was built with the x-ray crystal structure of *E. coli* GlpG (3) (PDB code: 2IC8; 2.1 Å resolution) embedded in a lipid bilayer lying on the xy-plane, with the z-axis normal to the membrane. The lipid bilayer was constructed using a mixture of POPE:POPG = 231:77 on the web-based CHARMM-GUI membrane builder (14). Then, the composite system (*i.e.*, GlpG and the lipid bilayer) was immersed in the TIP3P water solvent (15) followed by a charge neuralization and ionization with 150mM NaCl, which resulted in a final model of over 78,000 atoms in a box of $100\times100\times81$ Å^3. Inter- and intramolecular potential energies were enumerated based on the CHARMM36 force field (16). The nonbonding van der Waals and short-range electrostatic interactions were treated with a typical cutoff distance of 12 Å, while the long-range electrostatic contributions were evaluated with the particle-mesh Ewald method (17). All simulations were carried out using the NAMD2 software (18) massively parallelized on the GPU-accelerated IBM Power8 machine with a 2-fs time step in the semi-isotropic isobaric and isothermal (NPT) ensemble of 1 atm and 310 K, by which the membrane normal (z-axis) fluctuated independently from the lateral dimensions (xy-plane). The system was first subject to 10,000 steps of conjugate gradient energy minimization with restraints on lipids and GlpG to preserve their conformation and relative positions, followed by further pre-equilibration along 6 separated stages as the restraints gradually relaxed until no constraints applied. Then, we ran the MD of GlpG WT for ~150 ns. The final snapshot was employed as a starting structure for the 14 different variants as well as for WT. We obtained at least ~1.1 μs up to ~1.4 μs trajectories for WT and each variant.

Cavity Volume Analysis. We specified five distinct cavities in GlpG, numbered from Cavity I to V (**Fig. 2** and ***SI Appendix*** **Figs., S3** and **S5**). Cavity volumes were calculated with *trj_cavity* (19), a software for cavity identification and volume assessment which was developed using a grid-based neighbor searching algorithm. Using this tool, a cavity was first examined from a given seed coordinate, and its size was enumerated if the cavity existed with a grid resolution of 1.0 Å. Before assessment, the protein, *i.e.*, GlpG in each MD trajectory was first prepared to be aligned with respect to the initial input orientation for each cavity to be consistent among all frames for the same seed. We used the center of geometry of constituent residues in each cavity as the seed coordinates. Multiple cavities could be found as we move away from the seed, but we only considered the closest one in each cavity. Cavity volumes were then averaged over all available frames for WT and each variant.

Lipid Occupancy in Cavity. Cavity-filling mutations in membrane proteins can affect lipid solvation of cavities by directly changing cavity volume or indirectly through allosteric modulation. We analyzed the changes in lipid occupancy on all designated cavities upon mutation. Since cavity volume fluctuated over the simulation, so did the lipid molecules. We first specified the cavities in each frame as a set of grid points as described in **Cavity volume analysis** in ***SI Appendix, Methods***. Then, we measured the lipid occupancy for each cavity by counting the number of lipid heavy atoms within 1 Å of any grid points that defined the cavity.

Benchmark Test with Bacteriorhodopsin. To validate our method for evaluating the changes in cavity size upon mutation, we selected bacteriorhodopsin (bR) as our benchmarking system. In 2009, Joh et al. reported the energetic contribution of van der Waals packing by taking examples of a membrane protein (*i.e.*, bacteriorhodopsin) and a water-soluble protein (*i.e.*, T4-lysozyme) (20, 21). With bR, they examined six variants: one (V49A; PDB code: 3HAN) in-between TM2, TM3 and TM7, and five L94A (3HAO), L111A (3HAP), L148A (3HAQ), L148V (3HAR) and L152A (3HAS) in-between TM3, TM4, TM5 and TM6. Thus, we constructed seven MD simulation systems including WT (1PY6) and those variants (each PDB code is indicated above in the parenthesis) in the DMPC bilayer, which is similar to the experimental condition. Using the same MD simulation protocol as in GlpG, for each system, we began with structural minimization, followed by six short MD runs of pre-equilibration as gradually removing constraints imposed on protein and lipids. Then, we generated trajectories of up to ~1.4μs for each system with no constraints imposed as production runs. Next, we generated the time-dependent profile of the root-mean-square deviation (RMSD) for each system referring to the corresponding x-ray crystal structure. Taking the last 500 ns, we analyzed the cavity volume. In each system, the cavity volumes were measured for the cavities near the mutation sites. Five variants (L94A, L111A, L148A, L148V and L152A: group 1) shared a common cavity (Cavity I_{bR}), while V49A (group 2) formed the other (Cavity II_{bR}).

At our benchmarking level, we attempted to construct a simple linear response model to predict the difference unfolding free energy change ($\Delta\Delta G^{o}_{U,WT\text{-}Mut,Sim}$) of bR as a function of the volume changes of Cavity I_{bR} and II_{bR} for all variants as follows:

$$\Delta\Delta G^{o}_{U,WT\text{-}Mut,Sim}(m) = c_{I}\Delta V_{I,WT\text{-}Mut}(m) + c_{II}\Delta V_{II,WT\text{-}Mut}(m) + b \qquad \textbf{(Eq. S1)}$$

, where *m* designates a mutation type, $\Delta V_{I,WT\text{-}Mut}(m)$ and $\Delta V_{II,WT\text{-}Mut}(m)$ are the volume changes at Cavity I_{bR} and II_{bR} induced by the mutation, *i.e.*, $V_I(m) - V_I(WT)$ and $V_{II}(m) - V_{II}(WT)$, respectively, and c_I and c_{II} are the corresponding coefficients, which are determined from the model fitting with the constant, *b*, related to the change in water or lipid solvation upon mutation.

Examining the Equilibration of Protein and Lipids. Relaxation times of proteins in the membrane are expected to be longer than those in aqueous solution due to the slow lipid dynamics. To test the system equilibrium, we focused our observation on three parts: (1) protein, (2) lipids in the bulk, and (3) lipids in contact with protein. To test the equilibration of protein conformation, we monitored global structural fluctuations by calculating the heavy atom RMSD's during simulation until an enough number of conformations are obtained to reach equilibration (*i.e.*, ~500 ns). Next, to test the equilibration of lipid conformation in the bulk, we targeted lipid molecules located 40 Å away from the protein surface, by which on average 57 ± 3 lipid molecules (12 ± 1 POPG and 45 ± 2 POPE) were selected in each protein system. Then, we calculated the *RMSD* (τ) as a function of the time lag τ by averaging over all available lipid molecules in the bulk as follows:

$$RMSD(\tau) = \frac{1}{N_L}\sum_{i=1}^{N_L}\langle RMSD_i(t, t+\tau)\rangle_t \quad \textbf{(Eq. S2)}$$

, where N_L is the number of the selected lipid molecules, and $<RMSD_i(t, t+\tau)>_t$ is the heavy-atom root-mean square deviation between the *i*-th lipid conformations at the time *t* and $t+\tau$, averaged over the time *t*. Prior to RMSD calculation, the lipid conformations in comparison at each *t* and $t+\tau$ were structurally aligned with each other by transrotating the heavy-atom conformations. Lastly, for the interfacial lipids in contact with protein, we focused on how fast the lipid exchange would occur at the protein-lipid interface by measuring the lipid residence time using the autocorrelation function on time for the lipid heavy atom in contact with the protein as follows:

$$c(\tau) = \frac{1}{N_c}\sum_{i=1}^{N_c}\langle c_i(t, t+\tau)\rangle_t \quad \textbf{(Eq. S3)}$$

, where N_c is the number of contact events, and a single contact event is defined as a consecutive contact of a lipid with no non-contacting time gap longer than the lipid relaxation time measured above (*i.e.*, 20 ns). The autocorrelation function at the time τ of the *i*-th contact event, $<c_i(t, t+\tau)>_t$ is defined by $<q_i(t)q_i(t+\tau)/q_i^2(t)>_t$, the normalized product of heavy atom contact numbers of a lipid in the *i*-th contact event, $q_i(t)$ and $q_i(t+\tau)$ at two time moments (*t* and $t+\tau$), averaged over the time *t*.

Preparation of GlpG and Mutagenesis. Detailed procedures for constructing the DNA vector, and expression and purification of GlpG are described in the literature (22). Briefly, the TM domain of GlpG (residues 87-276) encoded in pET15b vector was expressed in *E. coli* BL21(DE3) RP strain (Agilent) with an N-terminal His$_6$-tag. Cells were grown at 37°C in LB media containing 100 μg/L ampicillin until OD$_{600nm}$ reached 0.6. Protein expression was induced with 0.5 mM isopropyl β-thiogalactopyranoside (IPTG, GoldBio), followed by additional cultivation at 15 °C for 16 h. GlpG was purified from the total membrane fraction obtained by ultracentrifugation (Beckman Coulter, Type 45 Ti rotor, 50,000 *g*, for 2 h) using Ni^{2+}-NTA affinity chromatography (Qiagen) after solubilization the membrane pellet with 1% *n*-dodecyl-β-D-maltoside (DDM, Anatrace). Site-directed mutagenesis for amino acid substitution was performed using the QuikChange Site-Directed Mutagenesis Kit (Agilent).

Biotin Labeling of GlpG. To label GlpG with the thiol-reactive biotin derivative with pyrene fluorophore, N-(5-(2-iodoacetamido)-6-oxo-6-(2-(+)-Biotin hydrazinyl)hexyl)-4-(pyren-1-yl)butanamide (BtnPyr-IA) (22), purified cysteine variants (G172C/267C or P95C/G172C) in 0.2% DDM, 50 mM Tris-(hydroxymethyl) aminomethane hydrochloride (TrisHCl), 200 mM NaCl and pH 8.0 were diluted to less than 100 μM and incubated with a ten-fold molar excess of Tris(2-carboxyethyl)phosphine hydrochloride (TCEP-HCl, Pierce) for 1 h at room temperature. Labeling reaction was initiated by adding 40 times molar excess of BtnPyr-IA dissolved in DMSO (~20 mg/ml) to the GlpG mixture during vortexing, and incubated at room temperature overnight in the dark. Excess free labels were removed by extensive washing of the proteins bound to Ni^{2+}-NTA affinity resin using 0.2% DDM, 50 mM TrisHCl, 200 mM NaCl and pH 8.0 solution. Labeled GlpG was dialyzed against 0.02% DDM, 50 mM TrisHCl, 200 mM NaCl, pH 8.0 buffer to remove imidazole. Typically, the labeling efficiency of BtnPyr-IA ranged from 1.5–2.2 as estimated from SDS-PAGE gel shift assay or comparison of the concentration of BtnPyr determined by pyrene absorbance (ε_{346nm} = 43,000 M·cm^{-1}) to the concentration of GlpG determined by DC protein assay (Bio-Rad) (22). Wild-type monovalent streptavidin (mSA-WT), and its variants mSA-S27A and mSA-S45A, in which mutations were made on the active subunit of tetrameric mSA to reduce biotin affinity, was prepared as described previously (23, 24). Each mSA variant contained a single-cysteine mutation S83C, to which the thiol-reactive dabcyl quencher (DABCYL Plus™ C2 maleimide, Anaspec) was conjugated for binding assay between mSA and GlpG-BtnPyr$_2$.

Expression and Purification of GlpG Substrate SN-LYTM2. For functional assay of GlpG, we used its proteolytic activity mediating sequence-specific cleavage of a transmembrane (TM) substrate, the second TM domain of the lactose permease of *E. coli* (LYTM2) (25) fused to staphylococcal nuclease (SN) (22). This construct was encoded in pET30a vector that contains the SN domain (26), TEV protease recognition site, and C-terminal His$_6$-tag (SN-TEV-LYTM2-His$_6$). In the LYTM2 region, the position which was five residues upstream from the scissile bond (P5 position) was substituted with cysteine for labeling with thiol-reactive, environment-sensitive fluorophore iodoacetyl-7-nitrobenz-2-oxa-1,3-diazol (IA-NBD amide, Setareh Biotech) (***SI Appendix,*** **Fig. S11A**). The construct was expressed in BL21(DE3) RP *E. coli* strain. The protein was expressed, purified and labeled as described previously (24).

Fluorescence-based Activity Assay for GlpG. Activity assay at room temperature was initiated by addition of 10 times molar excess of NBD-labeled SN-LYTM2 to purified GlpG variants. Fluorescence change, which indicates the transfer of the environment-sensitive NBD fluorophore from the hydrophobic micellar phase to the aqueous phase upon cleavage, was normalized to the control sample containing NBD-SN-LYTM2 without GlpG (***SI Appendix,*** **Fig. S11B**). To test the activity for water-soluble casein, Bodipy FL-labeled casein (0.15 mg/ml, Thermo-Fisher) was added to GlpG (5 μM) in DDM. The activity, which was measured at 37 °C, was represented by the initial slope of the fluorescence change *versus* time, indicating the substrate cleavage rate. Time-dependent changes of NBD or Bodipy FL fluorescence were monitored in 96-well plate using SpectraMax M5e plate reader (Molecular Devices) with excitation and emission wavelengths of 485 nm and 535 nm, respectively. As in **Fig. 2**, the relative activity denotes the activity ratio of a given GlpG variant without biotin labels to GlpG WT without biotin labels.

Obtaining a Binding Isotherm to Determine Thermodynamic Stability of GlpG Using Steric Trapping. Thermodynamic stability of GlpG in DDM micelles was determined by measuring the attenuated second binding of mSA labeled with dabcyl quencher (mSA$_{DAB}$) to GlpG doubly labeled with BtnPyr (172/267-BtnPyr$_2$ or 95/172-BtnPyr$_2$) at room temperature (***SI Appendix,*** **Fig. S9** and **S10**) (22). The readout for mSA$_{DAB}$ binding was quenching of pyrene fluorescence from BtnPyr labels by Förster resonance energy transfer (FRET). 1 μM of 172/267-BtnPyr$_2$ or 95/172-BtnPyr$_2$ was titrated with a mSA$_{DAB}$ variant possessing a reduced biotin binding affinity (22), mSA$_{DAB}$-S45A ($K_{d,biotin}$ = 9.0 ± 4.3 nM) or mSA$_{DAB}$-S27A ($K_{d,biotin}$ = 1.4 ± 0.9 nM) in 5 mM DDM, 0.25 mM TCEP, 20 mM sodium phosphate and 200 mM NaCl (pH 7.5). The titrated samples were transferred to a 96-well UV-compatible microplate, sealed with a polyolefin tape, and incubated for 2 days (for 172/267-BtnPyr$_2$) or 5 days (for 95/172-BtnPyr$_2$) at room temperature. Quenching of pyrene monomer fluorescence at 390 nm was monitored with an excitation wavelength of 345 nm on SpectraMax M5e plate reader. Data were averaged from four readings. Non-specific FRET between pyrene and dabcyl was negligible (22).

Fitting of Binding Isotherm to Determine Thermodynamic Stability of GlpG. Fitting equation to obtain thermodynamic stability of GlpG using steric trapping was based on the following reaction scheme (22, 27):

$$\mathrm{F}\cdot\mathrm{mSA}\xrightleftharpoons{K_{\mathrm{U}}}\mathrm{U}\cdot\mathrm{mSA}\text{, where }K_{\mathrm{U}}=\frac{[\mathrm{U}\cdot\mathrm{mSA}]}{[\mathrm{F}\cdot\mathrm{mSA}]}\qquad\textbf{(Eq. S4)}$$

$$\mathrm{U}\cdot\mathrm{mSA}+\mathrm{mSA}\xrightleftharpoons[K_{\mathrm{d,biotin}}]{}\mathrm{U}\cdot 2\mathrm{mSA}\text{, where }K_{\mathrm{d,biotin}}=\frac{[\mathrm{U}\cdot\mathrm{mSA}][\mathrm{mSA}]}{[\mathrm{U}\cdot 2\mathrm{mSA}]}\qquad\textbf{(Eq. S5)}$$

Fitting equation for the second mSA binding phase was:

$$F=\frac{1}{[1+\left(K_{\mathrm{d,biotin}}+\dfrac{K_{\mathrm{d,biotin}}}{K_{\mathrm{U}}}\right)\dfrac{1}{[\mathrm{mSA}]}]}\left(F_{\infty}-F_{o}\right)+F_{o}\qquad\textbf{(Eq. S6)}$$

, where F is the measured fluorescence intensity, and F_0 and F_∞ are the fluorescence intensities from GlpG labeled with BtnPyr at [mSA] = 0 and at the saturated bound level, respectively. [mSA] is the total mSA concentration, $K_{\mathrm{d,biotin}}$ is the dissociation constant for unhindered biotin binding affinity of mSA (22), and K_{U} is the equilibrium constant for unfolding of GlpG. After obtaining the fitted K_{U}, the thermodynamic stability was calculated using the equation $\Delta G^{\circ}_{\mathrm{U}} = -RT\ln K_{\mathrm{U}}$.

On the Precision of $\Delta G^{\circ}_{\mathrm{U}}$ Determined by Steric Trapping. Our steric trapping approach allows precise measurement of $\Delta G^{\circ}_{\mathrm{U}}$ because: *i)* the attenuated second binding of mSA, which is coupled to unfolding and reflects $\Delta G^{\circ}_{\mathrm{U}}$, can be measured with a high sensitivity using Förster resonance energy transfer between BtnPyr label and quencher-labeled mSA; *ii)* the binding affinity of mSA to biotin labels can be controlled over a wide range ($K_{\mathrm{d,biotin}} = 10^{-9}$ to 10^{-5} M) by mutation on mSA (22). Thus, by an optimal choice of an mSA variant, small differences in $\Delta G^{\circ}_{\mathrm{U}}$ can be differentiated with typical standard errors in $\Delta\Delta G^{\circ}_{\mathrm{U,WT\text{-}Mut}}$ less than ±0.2 kcal/mol. $\Delta G^{\circ}_{\mathrm{U}}$'s of GlpG variants were determined in DDM micelles (***SI Appendix,*** **Fig. S10**).

Double Mutant Cycle Analysis. To measure the pairwise interaction energies between cavity-filled mutation sites, double-mutant cycle analysis was employed (28). A double-mutant cycle involves wild-type protein (WT), two single variants and the corresponding double variant. If the change in thermodynamic stability ($\Delta G^{\circ}_{\mathrm{U}}$) upon a double mutation ($\Delta\Delta G^{\circ}_{\mathrm{U,XY\text{-}X'Y}}+\Delta\Delta G^{\circ}_{\mathrm{U,X'Y\text{-}X'Y'}}$) differs from the sum of the changes due to individual single mutations ($\Delta\Delta G^{\circ}_{\mathrm{U,XY\text{-}XY'}} + \Delta\Delta G^{\circ}_{\mathrm{U,XY\text{-}X'Y}}$), the two residues in WT are coupled and the magnitude of the difference (interaction energy: $\Delta\Delta G_{\mathrm{Inter}}$) is related to the strength of interaction between them. X and Y denote wild-type residues of interest and X' and Y' designate the substituted residues for X and Y, respectively.

$$\begin{aligned}\Delta\Delta G_{\mathrm{Inter}} &= -\left[(\Delta\Delta G^{\circ}_{\mathrm{U,XY\text{-}XY'}} + \Delta\Delta G^{\circ}_{\mathrm{U,XY\text{-}X'Y}}) - (\Delta\Delta G^{\circ}_{\mathrm{U,XY\text{-}X'Y}} + \Delta\Delta G^{\circ}_{\mathrm{U,X'Y\text{-}X'Y'}})\right]\\ &= -\left[(\Delta\Delta G^{\circ}_{\mathrm{U,XY\text{-}XY'}} + \Delta\Delta G^{\circ}_{\mathrm{U,XY\text{-}X'Y}}) - (\Delta\Delta G^{\circ}_{\mathrm{U,XY\text{-}XY'}} + \Delta\Delta G^{\circ}_{\mathrm{U,XY'\text{-}X'Y'}})\right]\end{aligned}\qquad\textbf{(Eq. S7)}$$

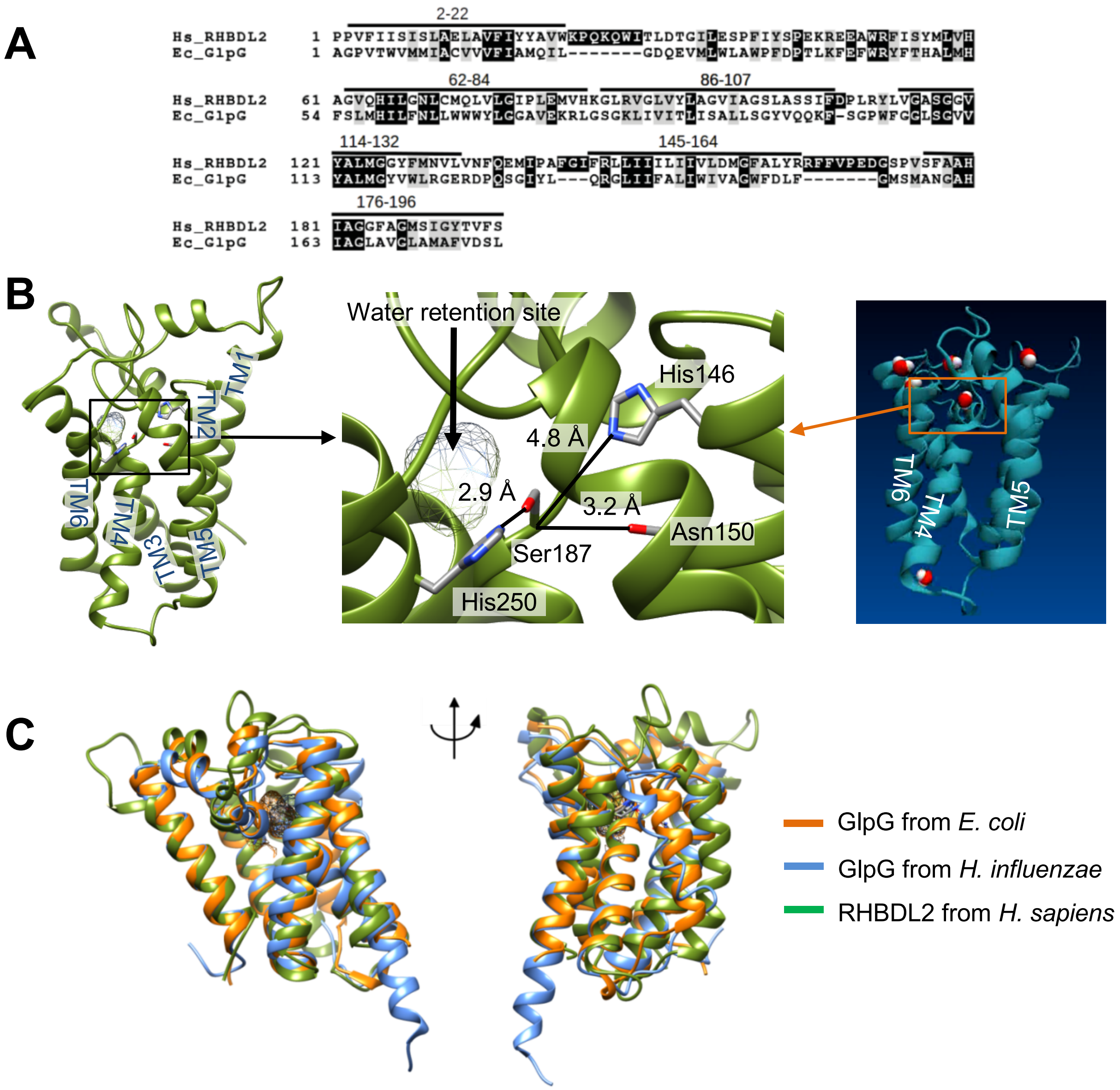

Fig. S1. Structural modeling of human rhomboid protease RHBDL2. ***(A)*** The sequence alignment of human rhomboid protease RHDBL2 (residues 71–266 spanning TM1–TM6 with TM7 truncated) and *E. coli* GlpG (residues 93–270). The predicted six TM helices are marked with the residue numbers (starting from 1). ***(B)*** The structural model of RHBDL2 obtained by homology modeling using the Rosetta Membrane program and MD simulation in a POPC bilayer (***SI Appendix*, Methods**). The validity of the modeled structure was evaluated using three aspects: (1) the spatial proximity among the catalytically important residues, *i.e.*, the catalytic dyad (Ser187-His250: $d_{\mathrm{His250N\varepsilon\text{-}Ser187O\gamma}}$ = 2.9 Å; 2.7 Å for *E. coli* GlpG) and the oxyanion hole ($d_{\mathrm{His146N\varepsilon\text{-}Ser187C\alpha}}$ = 4.8 Å; 5.7 Å for *E. coli* GlpG; $d_{\mathrm{Asn150O\delta\text{-}Ser187C\alpha}}$ = 3.2 Å; 4.0 Å for *E. coli* GlpG); (2) the presence of the water-retention site near the dyad that is known to be critical in the function and found in the crystal structures of GlpG of *E. coli* and *H. influenzae* (Cavity II in **Fig. S3**); (3) the penetration and residence of several water molecules near the active site during MD simulation. (*Right*) A structural snapshot showing the water molecules near the active site. ***(C)*** Superimposed structures of *E. coli* GlpG (PDB code: 3B45), *H. Influenzae* GlpG (2NR9) and human RHBDL2. The RMSD's of the C_{α} pairs were 1.17 Å between 3B45 and 2NR9, and 1.06 Å between 2NR9 and RHBDL2.

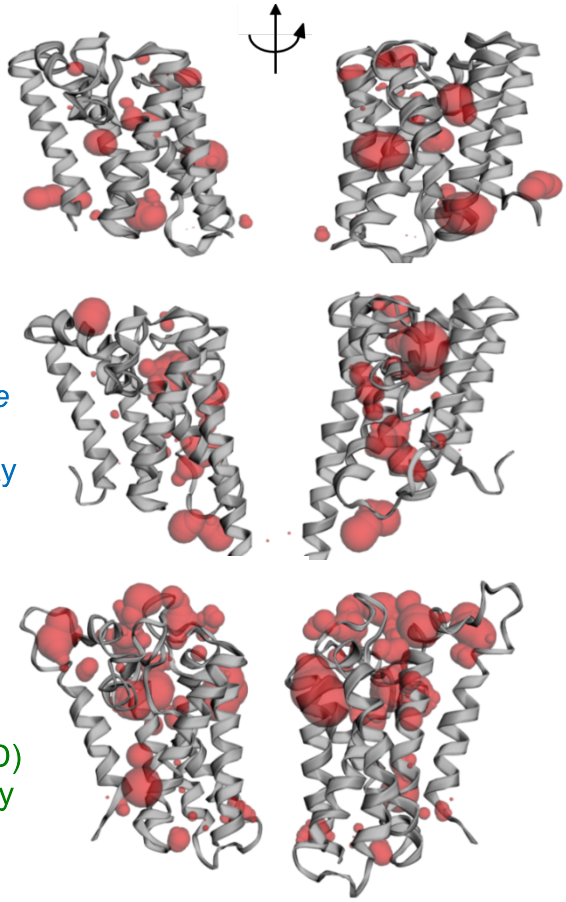

	***Number of Cavities per* 100 AAs**	***PD***
GlpG *E. coli* (1.9 Å)	13.4	0.724
GlpG *H. influenzae* (2.2 Å) 40.1% identity	8.6	0.737
RHBDL2 *H. sapiens* (RosettaM/MD) 26.2% identity	19.1	0.702

Fig. S2. Cavities in rhomboid proteases. The spatial distribution of the cavities in *E. coli* GlpG (3B45, resolution: 1.9 Å), *H. influenzae* GlpG (2NR9, resolution: 2.2 Å) and human RHBDL2 (modeled, see **Fig. S1**) obtained on the CASTp server using the 1.4-Å- (GlpG of *E. coli* and *H. influenzae*) or 1.0-Å-radius probe (RHBDL2). Number of cavities and internal packing density (PD) of each rhomboid protease are shown.

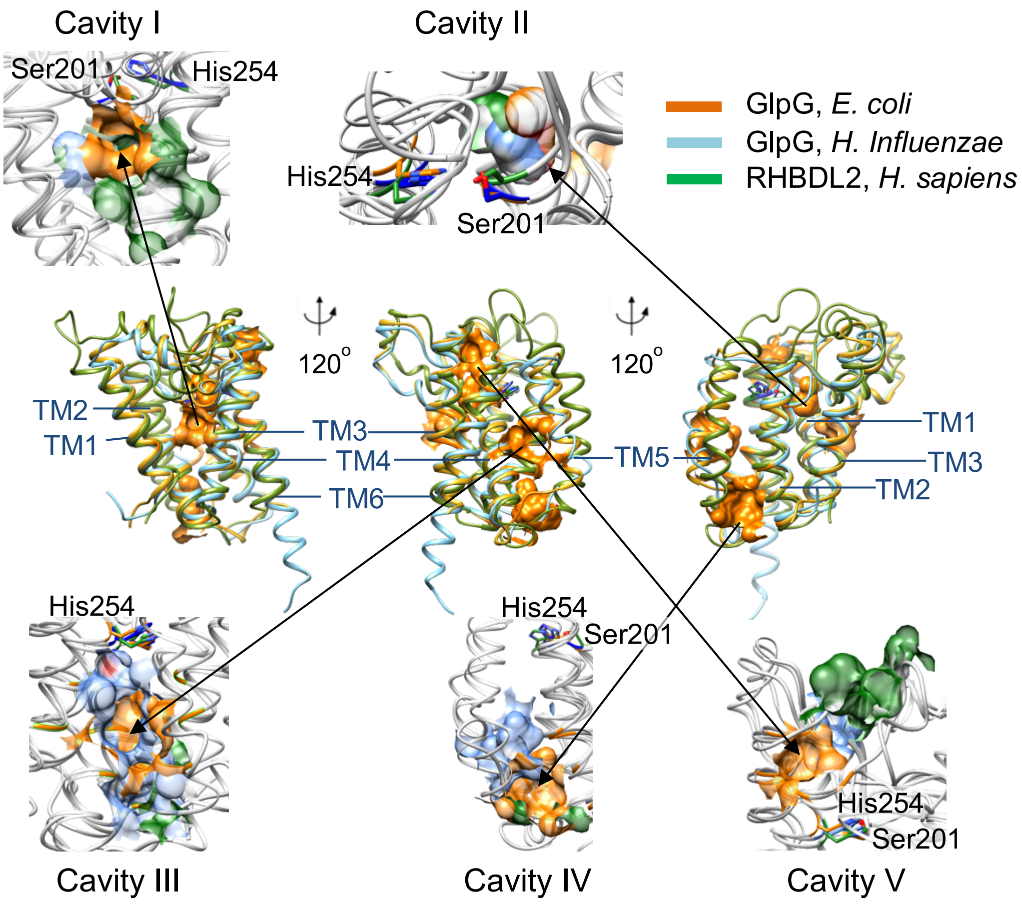

Fig. S3. Common cavities in the three rhomboid proteases.

Spatially overlapping cavities in the rhomboid structures, GlpG of *E. coli* (PDB code: 3B45), GlpG of *H. influenzae* (PDB code: 2NR9) and human rhomboid RHBDL2 (modeled). The backbones of the three rhomboid proteases are superimposed using the Matchmaker tool in the UCSF Chimera program. In the middle row, only the cavities in *E. coli* GlpG are shown.

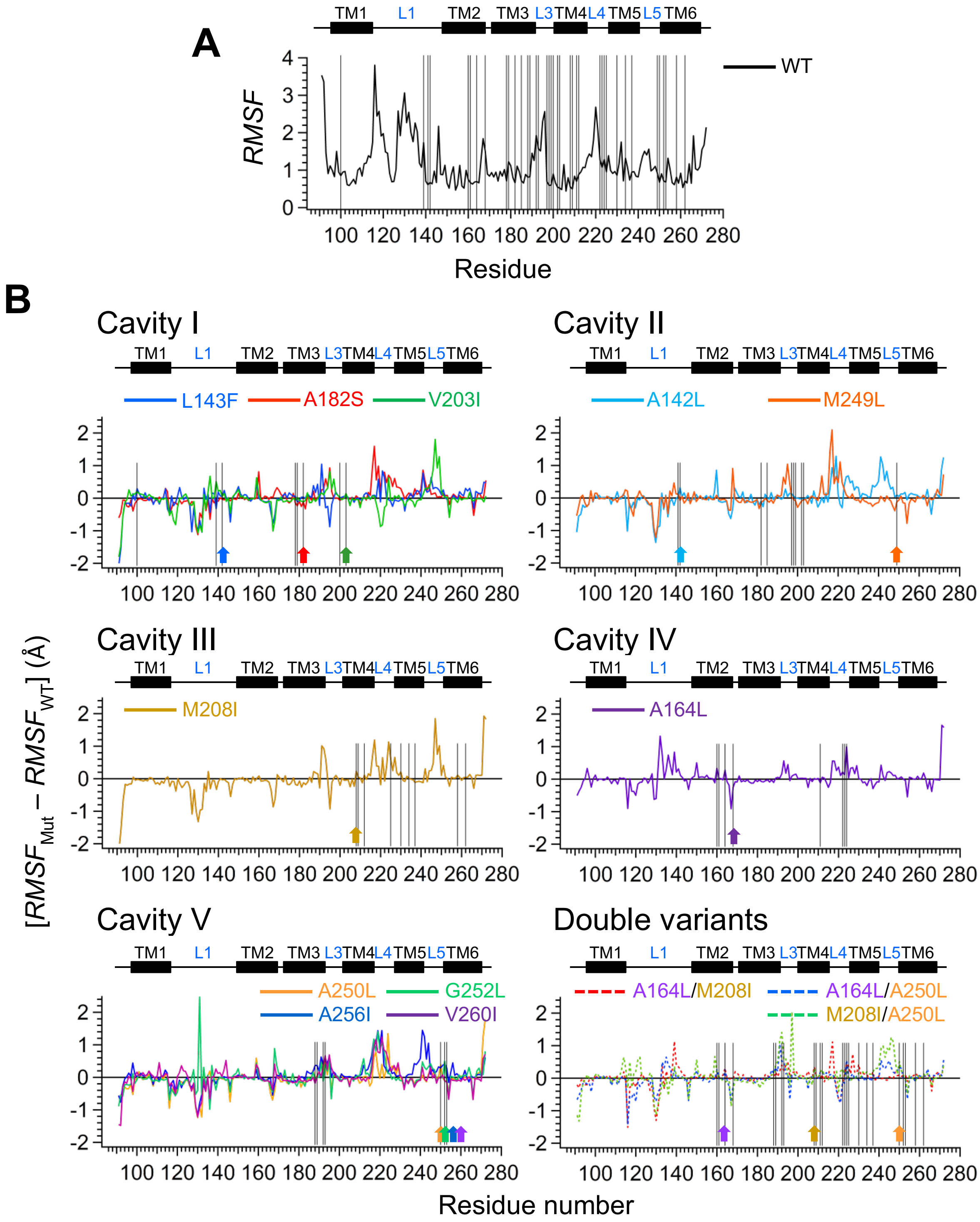

Fig. S4. The root-mean-square-fluctuations (RMSF's) of *E. coli* GlpG WT and variants during MD simulation in an explicit bilayer (POPE:POPG, molar ratio = 3:1) and water. *(A)* The residue RMSF's of WT. Vertical lines indicate the residues that contact the five cavities targeted for mutation. ***(B)*** The difference RMSF's between WT and each variant. Vertical lines indicate the residues surrounding the designated cavity and the upward arrows indicate the sites of mutation in each variant.

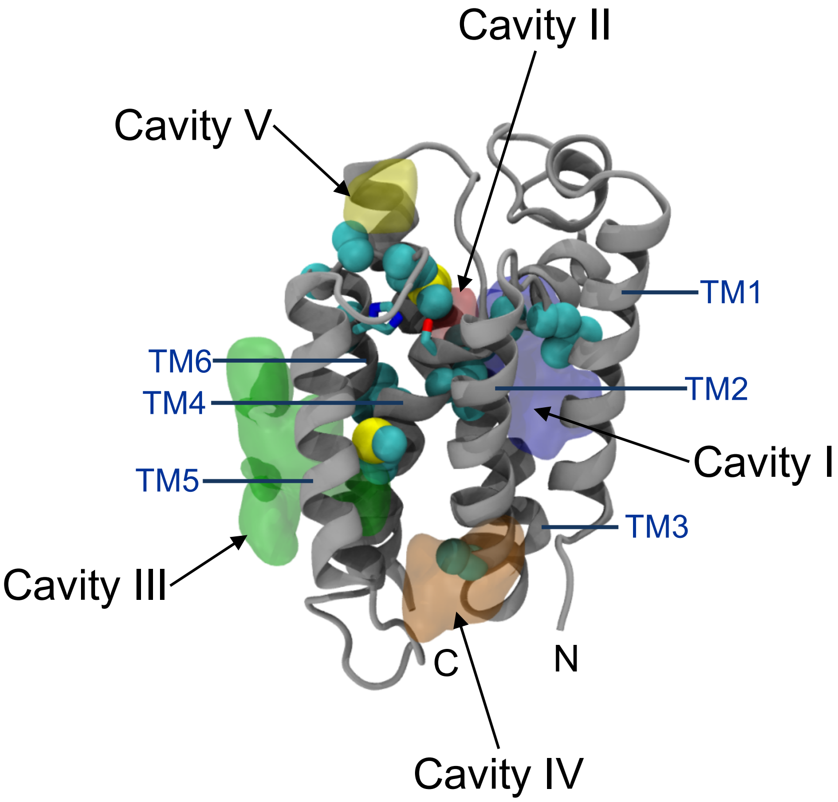

Fig. S5. The major cavities in a structural snapshot of GlpG WT during MD simulation. Each cavity is shown as a void volume which is present at least over 10% of the simulation time. The residues targeted for cavity-filling mutation are shown in the spheres.

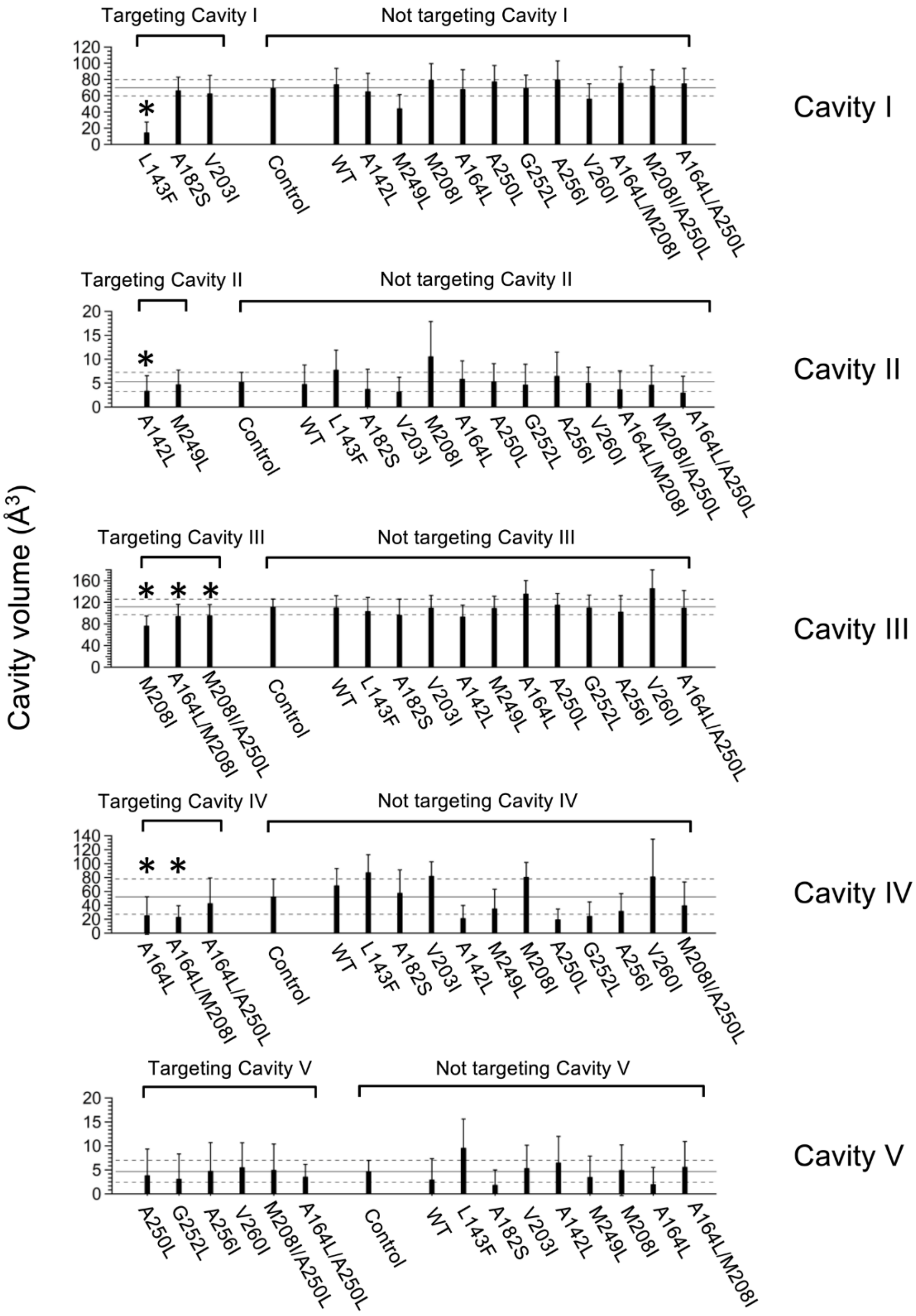

Fig. S6. Analysis of the cavity volume from MD simulation. The volume of each cavity in WT and variants. Each value represents the volume averaged over all time frames in MD simulation ($\langle V_{\mathrm{Cav}} \rangle$). Each error bar represents the standard deviation of the volume fluctuation. The "Control" indicates the average of the $\langle V_{\mathrm{Cav}} \rangle$ values for a designated cavity in WT and the variants that do not contain a mutation in that cavity (*i.e.*, $\langle\langle V_{\mathrm{Cav}} \rangle\rangle_{\text{not-targeted}}$, solid horizontal lines). The dashed horizontal lines denote the standard deviation of the $\langle V_{\mathrm{Cav}} \rangle$ values ($\langle\langle V_{\mathrm{Cav}} \rangle\rangle_{\text{not-targeted}} \pm \sigma_{\langle V\_\mathrm{Cav} \rangle \text{not-targeted}}$). The mutations that reduce the $\langle V_{\mathrm{Cav}} \rangle$ value lower than $\langle\langle V_{\mathrm{Cav}} \rangle\rangle_{\text{not-targeted}} - \sigma_{\langle V\_\mathrm{Cav} \rangle \text{not-targeted}}$ are regarded as improving the packing in the cavity and marked with asterisks.

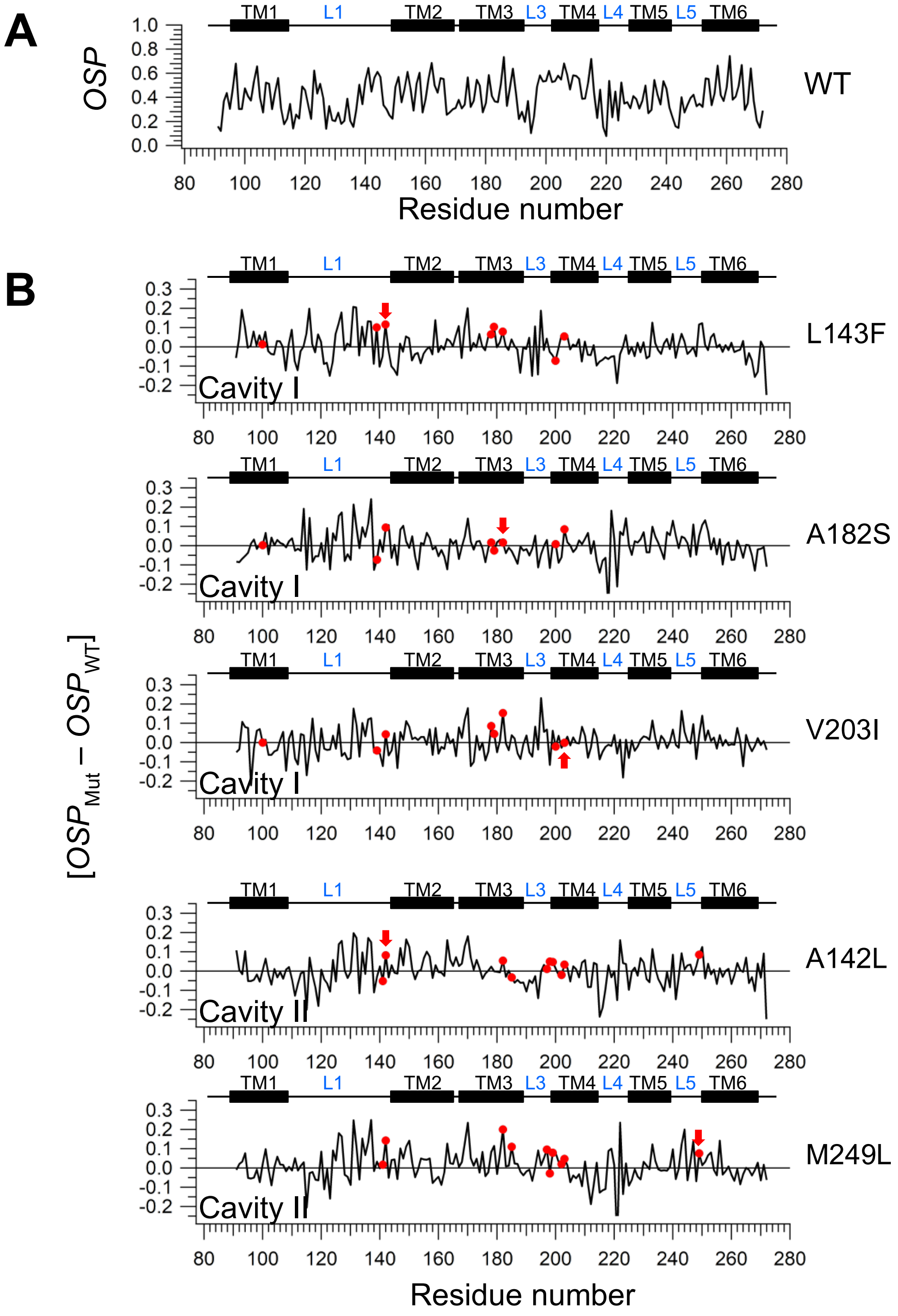

Fig. S7. Packing of GlpG WT and variants measured by the occluded surface. ***(A)*** The occluded surface packing (*OSP*) values of GlpG WT(29). The analysis was carried out using the Occluded Surface program on the last structural snapshots in the MD simulations of WT and variants. ***(B)*** The difference *OSP* values between WT and each variant. In each plot, the residues surrounding the designated cavity are marked with red dots and the mutation site in each variant is pointed with an arrow. A positive value indicates improved packing around the residue.

Continued in the next page

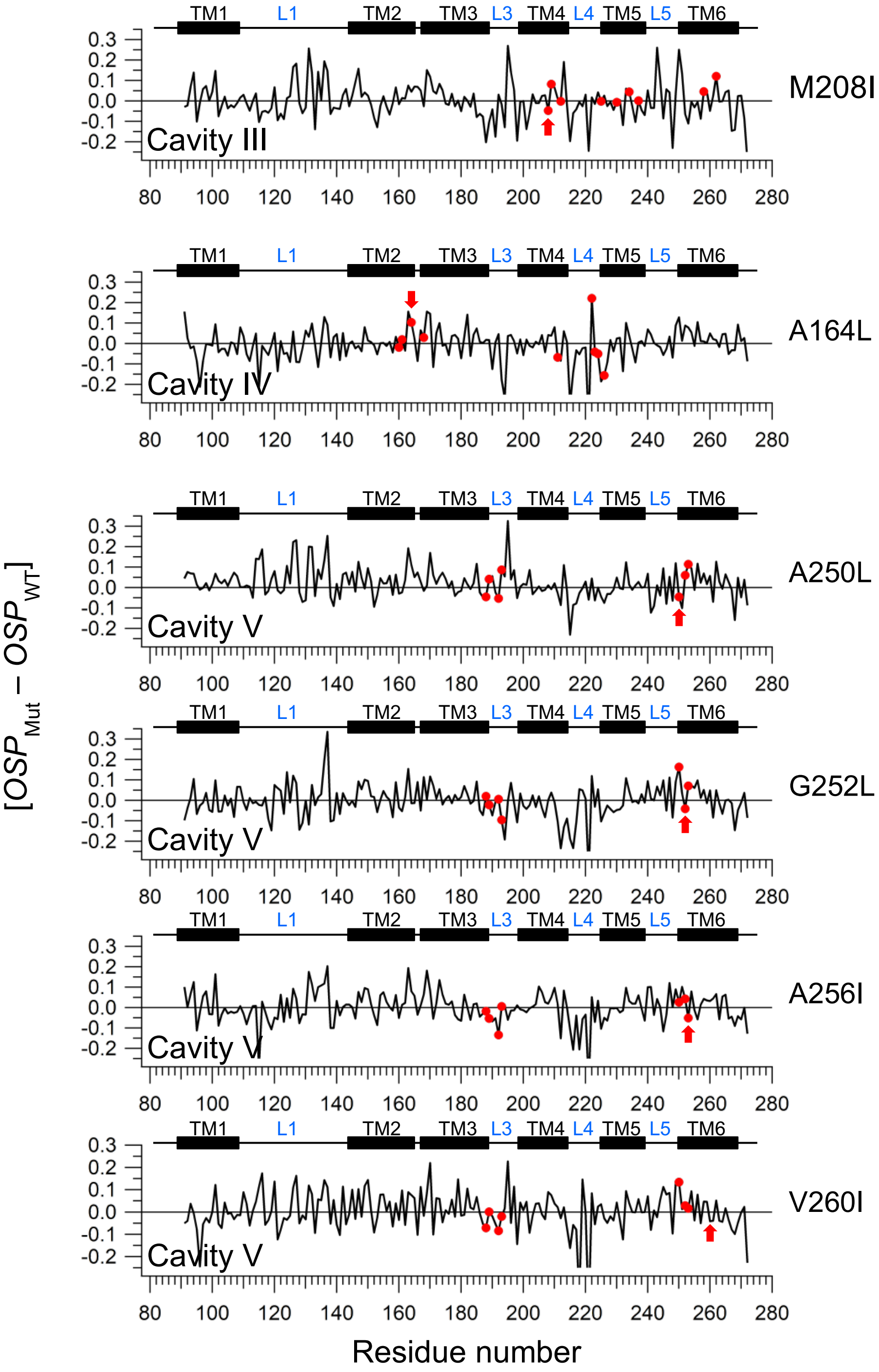

Continued Fig. S7B: Packing of GlpG WT and variants measured by the occluded surface.

Continued in the next page

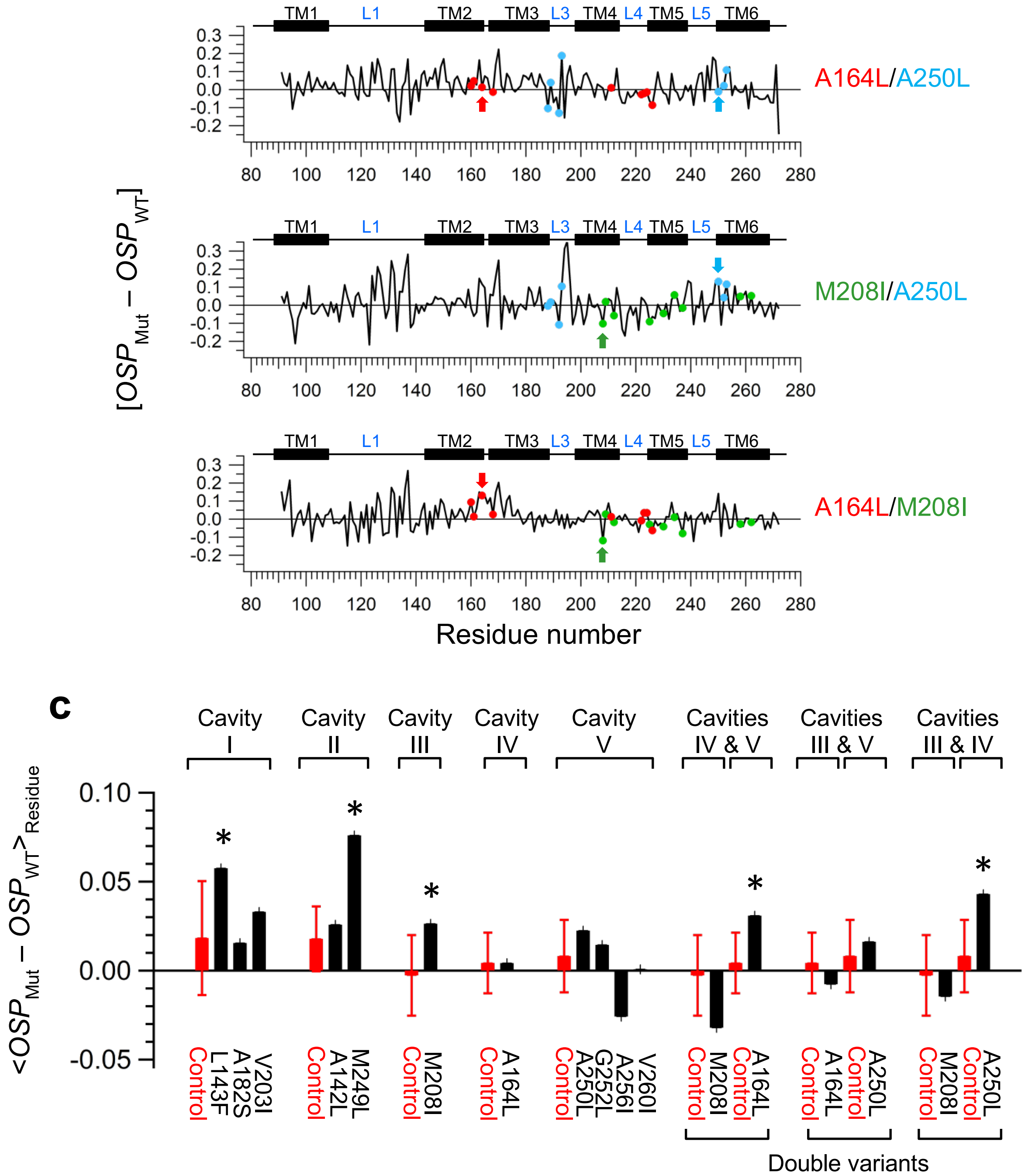

Continued Fig. S7B and S7C: Packing of GlpG WT and variants measured by the occluded surface. ***(C)*** The influence of cavity-filling mutations on the packing in the cavities targeted for mutation. For each variant, the difference *OSP* value averaged over the residues surrounding each targeted cavity ($<OSP_{\mathrm{Mut}} - OSP_{\mathrm{WT}}>_{\mathrm{Residue}}$) is plotted. In “Control” (red), the average of the $<OSP_{\mathrm{Mut}} - OSP_{\mathrm{WT}}>_{\mathrm{Residue}}$ values over WT and the variants which do not contain a mutation in the designated cavity ($<<OSP_{\mathrm{Mut}} - OSP_{\mathrm{WT}}>_{\mathrm{Residue}}>_{\mathrm{not\text{-}targeted}}$) and its standard deviation ($\sigma_{<OSP\_\mathrm{Mut} - OSP\_\mathrm{WT}>\mathrm{Residue,not\text{-}targeted}}$) are shown. The mutations whose $<OSP_{\mathrm{Mut}} - OSP_{\mathrm{WT}}>_{\mathrm{Residue}}$ values exceed the upper limit of the corresponding control ($<<OSP_{\mathrm{Mut}} - OSP_{\mathrm{WT}}>_{\mathrm{Residue}}>_{\mathrm{not\text{-}targeted}} + \sigma_{<OSP\_\mathrm{Mut} - OSP\_\mathrm{WT}>\mathrm{Residue,not\text{-}targeted}}$) indicate improved packing and are marked with asterisks.

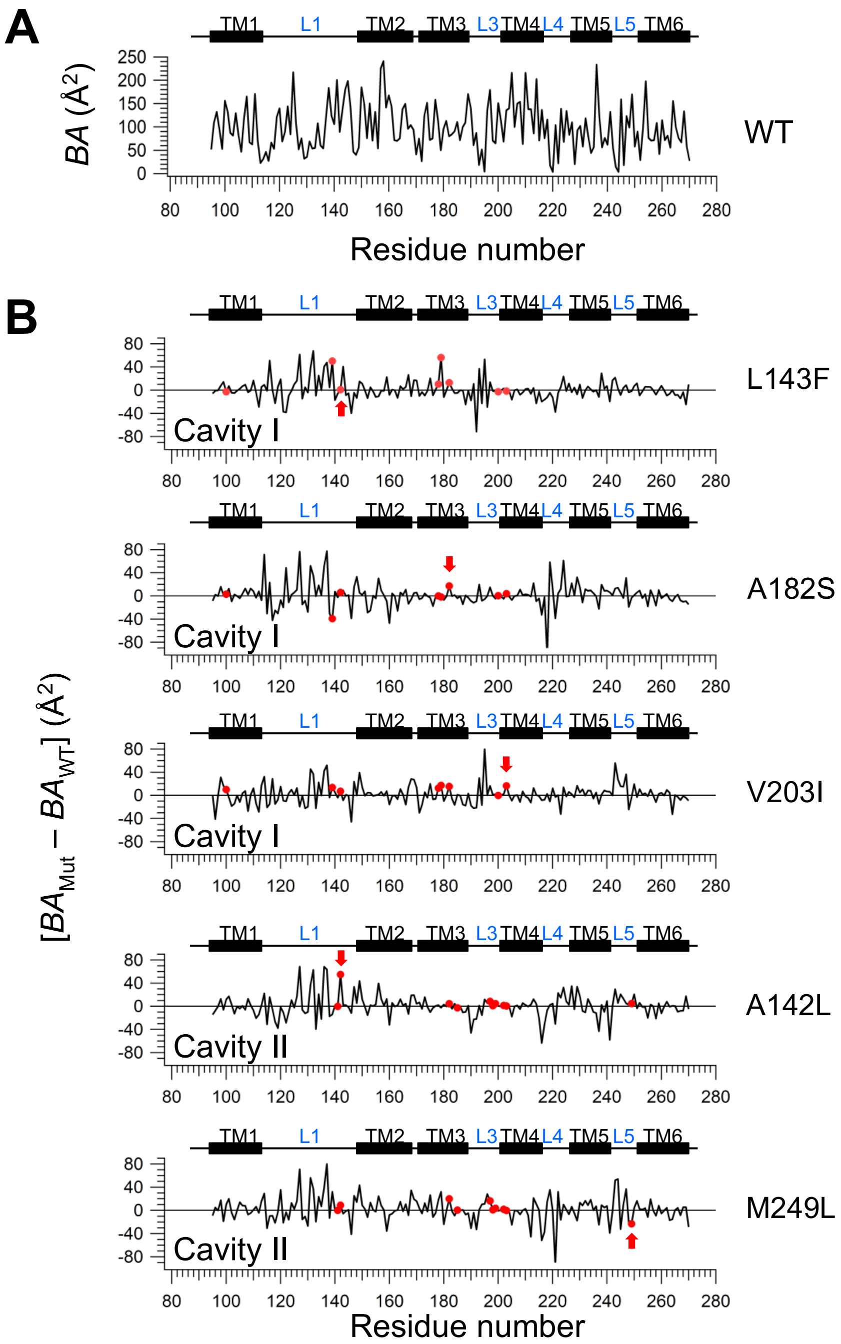

Fig. S8: Packing of GlpG WT and variants measured by the buried surface area (*BA*). *(A)* The residue solvent-inaccessible surface areas of GlpG WT. The buried area for each residue was obtained from the last structural snapshots in the MD simulations, using the equation, *Buried surface area* = *Total residue surface area* – *Solvent accessible residue surface area*, and the 1.4-Å-radius probe. ***(B)*** The difference buried surface area between WT and each variant. In each plot, the residues surrounding the designated cavity are marked with red dots and the mutated site is pointed with an arrow. A positive value indicates improved packing around the residue.

Continued in the next page

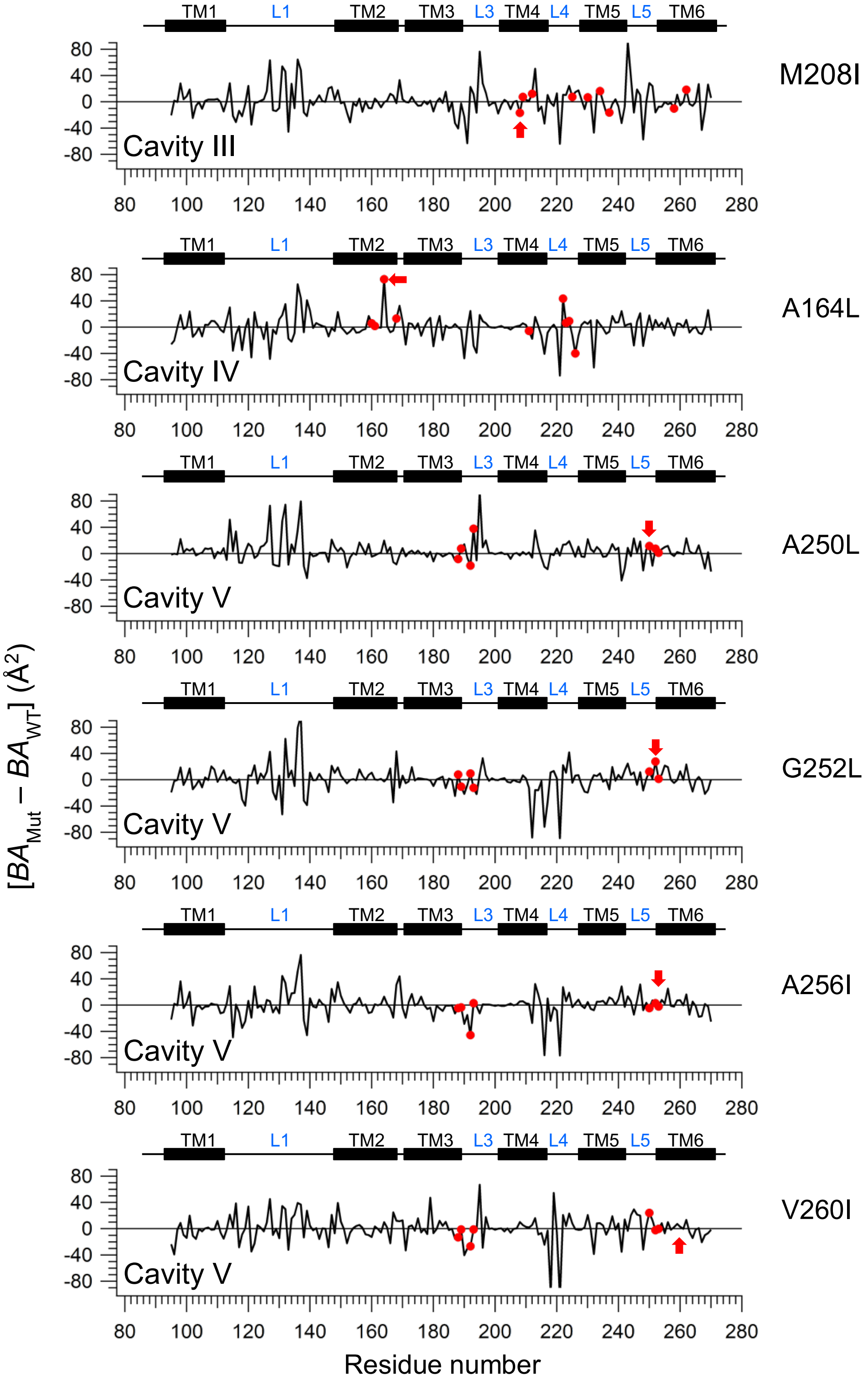

Continued Fig. S8B: Packing of GlpG WT and variants measured by the buried surface area.

Continued in the next page

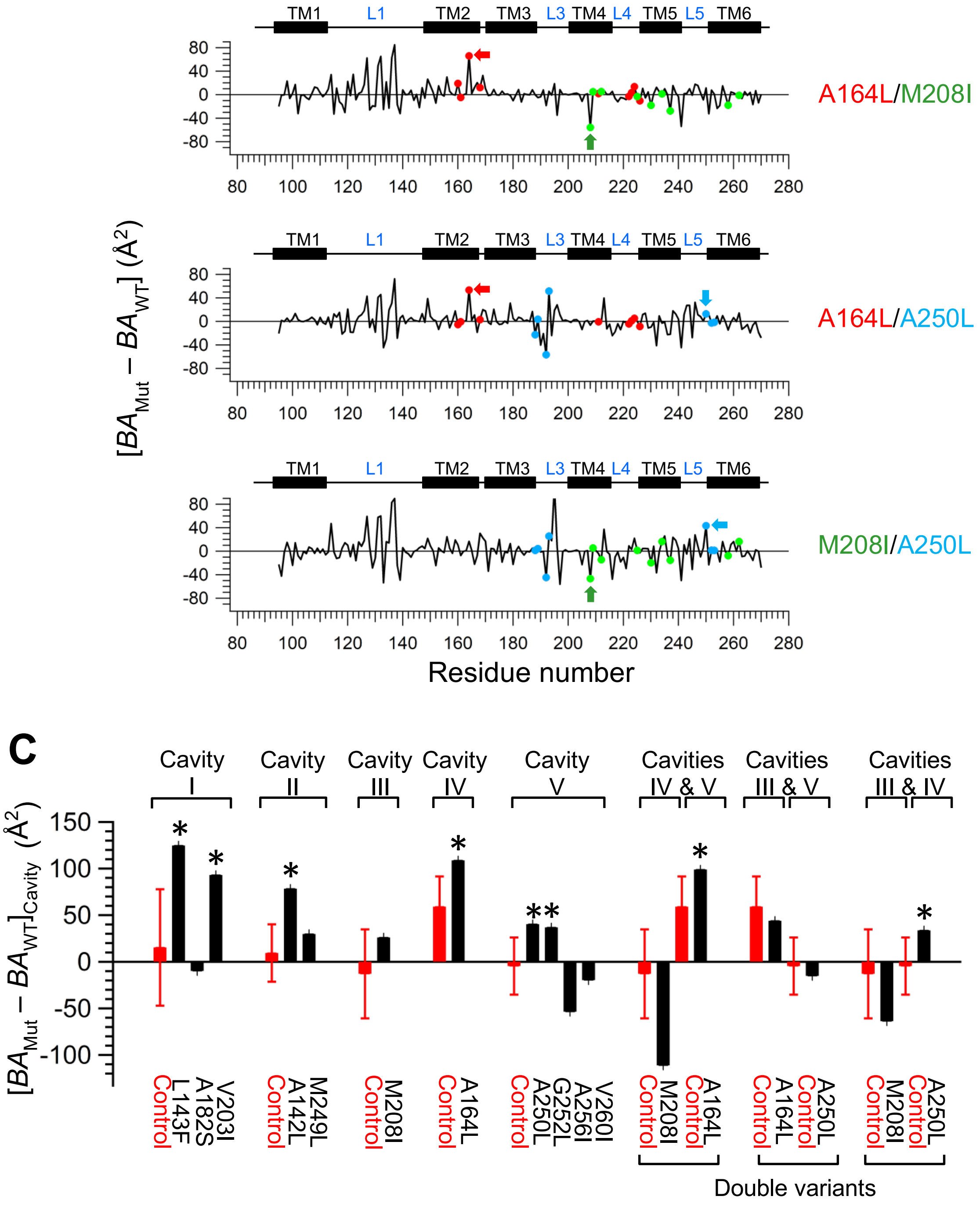

Continued Fig. S8B and S8C: Packing of GlpG WT and variants measured by the buried surface area. ***(C)*** For each mutation, the sum of the difference buried surface areas of the residues surrounding each targeted cavity ($[BA_{\mathrm{Mut}} - BA_{\mathrm{WT}}]_{\mathrm{Cavity}}$) is plotted. In "Control" (red), the average of the $[BA_{\mathrm{Mut}} - BA_{\mathrm{WT}}]_{\mathrm{Cavity}}$ values over WT and the variants which do not contain a mutation in the designated cavity ($\langle [BA_{\mathrm{Mut}} - BA_{\mathrm{WT}}]_{\mathrm{Cavity}} \rangle_{\text{not-targeted}}$) and its standard deviation ($\sigma_{[BA\_\mathrm{Mut} - BA\_\mathrm{WT}]\mathrm{Cavity,not\text{-}targeted}}$) are shown. The mutations whose $[BA_{\mathrm{Mut}} - BA_{\mathrm{WT}}]_{\mathrm{Cavity}}$ values exceed the upper limit of the corresponding control ($\langle [BA_{\mathrm{Mut}} - BA_{\mathrm{WT}}]_{\mathrm{Cavity}} \rangle_{\text{not-targeted}} + \sigma_{[BA\_\mathrm{Mut} - BA\_\mathrm{WT}]\mathrm{Cavity,not\text{-}targeted}}$, σ: the standard deviation) indicate improved packing and are marked with asterisks.

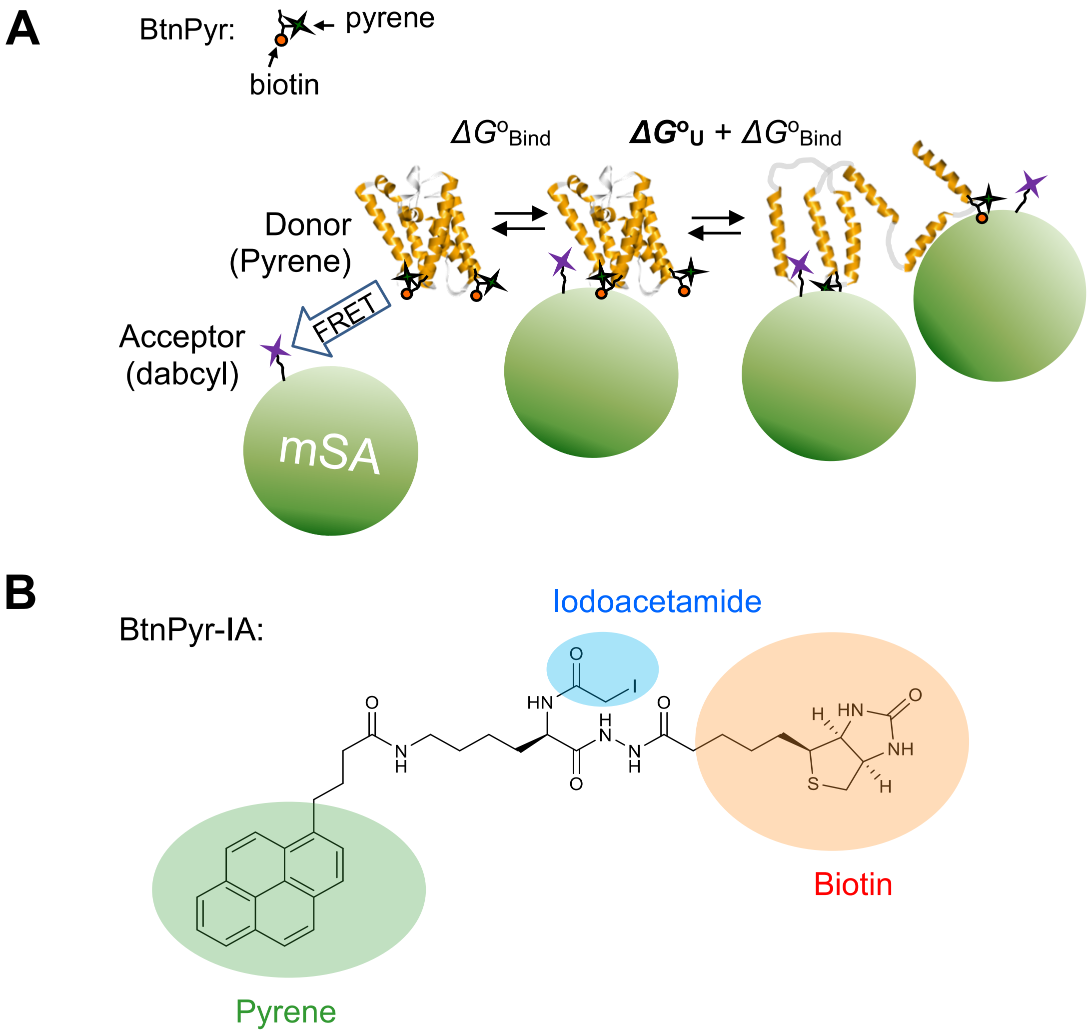

Fig. S9: Principles of steric trapping to measure the thermodynamic stability (ΔG^{o}_{U}) of GlpG. ***(A)*** FRET strategy to measure binding of monovalent streptavidin (mSA) to a double-biotin variant of GlpG. GlpG is doubly biotinylated with BtnPyr-IA (**Fig. S9B**). Single-cysteine variant of mSA (S83C) conjugated to the nonfluorescent quencher dabcyl (mSA_{DAB}) was used. The first mSA binds either biotin label with intrinsic binding affinity (ΔG^{o}_{Bind}). Because of steric hindrance between bulky mSA molecules, the second mSA binds only when native tertiary contacts are unraveled by transient unfolding. Hence, binding of the second mSA is attenuated depending on the stability of the target protein ($\Delta G^{o}_{Bind} + \Delta G^{o}_{U}$). By adjusting the biotin affinity of mSA by mutation, unfolding and binding reactions can be reversibly controlled, and ΔG^{o}_{U} of the target protein is obtained by monitoring binding of the second mSA or protein unfolding. ***(B)*** The thiol-reactive biotin derivative with the pyrene fluorophore used in this study.

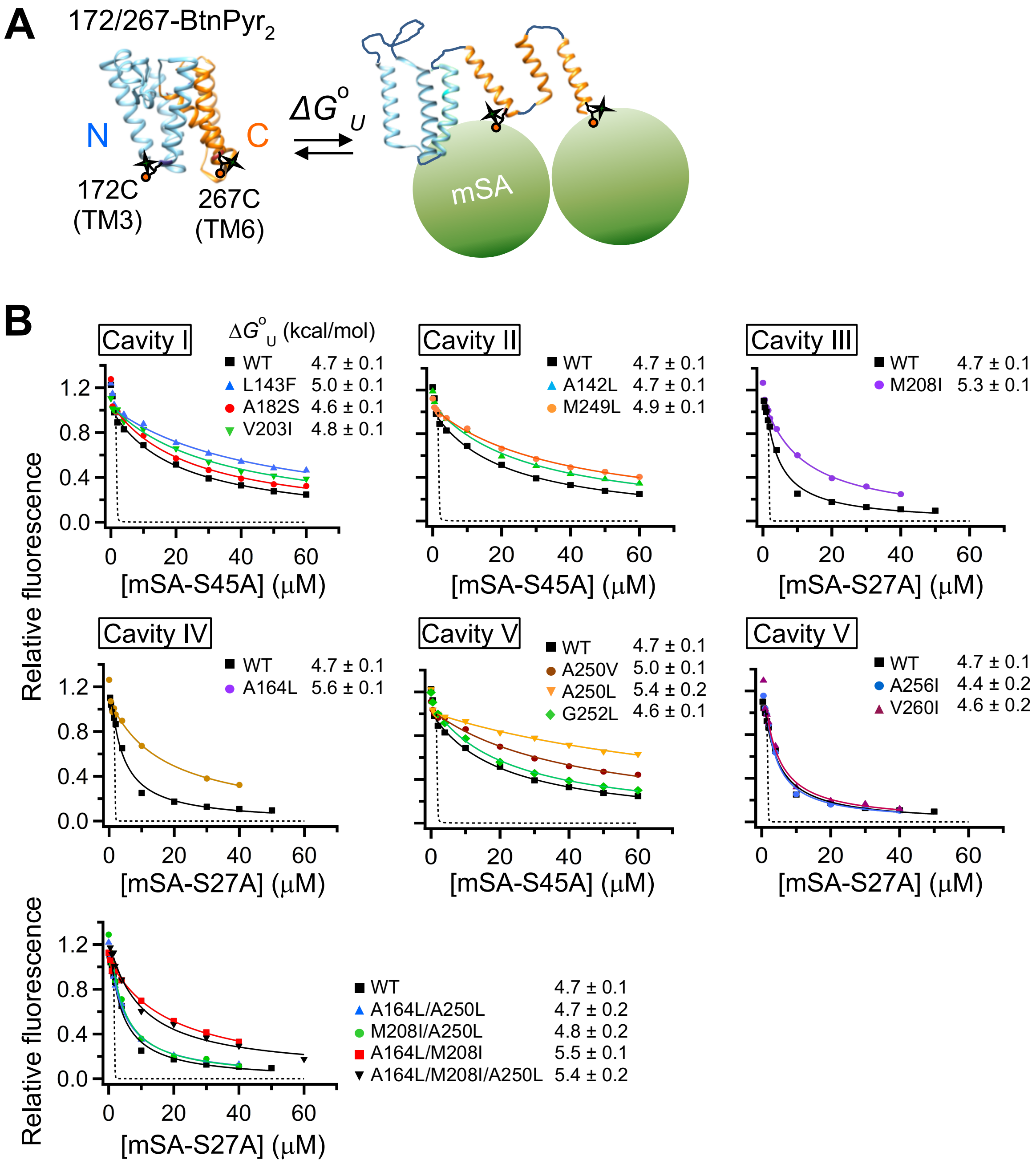

Fig. S10: Thermodynamic stability of the cavity-filled variants measured by steric trapping in DDM micelles. ***(A)*** Double-cysteine GlpG variants were labeled with thiol-reactive fluorescent biotin derivative BtnPyr-IA at 172C/267C (*i.e.*, 172/267-BtnPyr$_2$). The unfolded state was trapped by double binding of mSA. ***(B)*** Binding isotherms between double-biotin variants of GlpG (1 μM) and mSA (varied) measured by FRET (see **Fig. S9A**) to determine ΔG^{o}_{U}. When a mSA variant with weaker biotin affinity (mSA-S27A or mSA-S45A) is used, the first mSA binds either biotin label with intrinsic binding affinity (dashed lines in each plot). Binding of the second mSA is attenuated depending on the stability of the GlpG variant. ΔG^{o}_{U}'s were obtained by fitting the attenuated second binding to **Eq.'s S4 to S6** in ***SI Appendix,*** **Methods**. In each plot, the fluorescence intensity was normalized to the total intensity change of the second binding phase. The more attenuated second binding indicates the higher stability of GlpG (*i.e.*, larger ΔG^{o}_{U}).

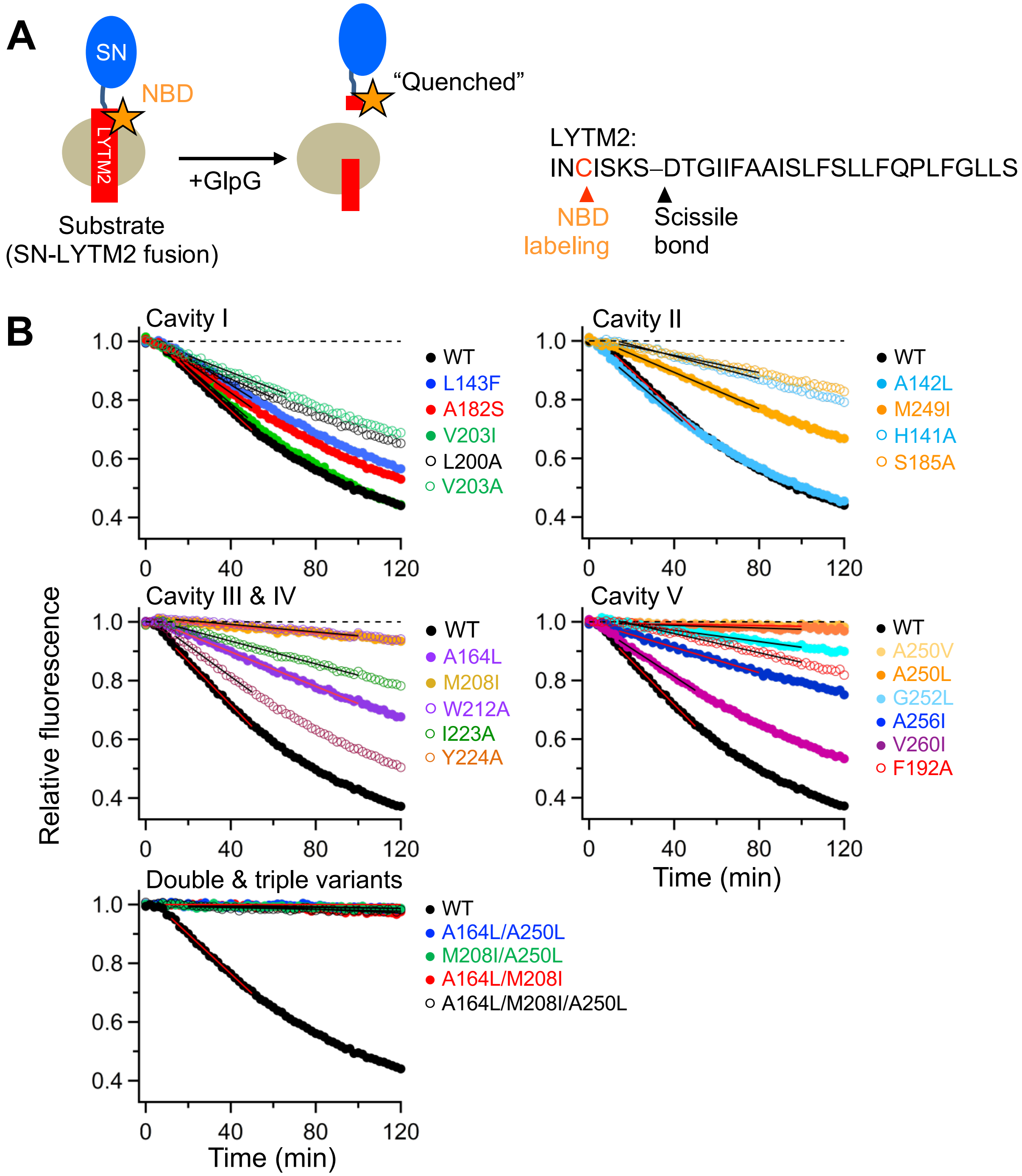

Fig. S11: Activity assay of GlpG WT and variants using the membrane-bound substrate LYTM2 in DDM micelles. ***(A)*** Principle of the fluorescence-based assay to precisely measure the proteolytic activity of GlpG. Cleavage of the model substrate NBD-labeled LYTM2 fused to staphylococcal nuclease domain induces quenching of the fluorescence from the environment-sensitive fluorophore NBD, which is transferred from the nonpolar micellar phase to the bulk aqueous phase. ***(B)*** Time-dependent cleavage of LYTM2 (10 μM) by GlpG WT and variants (1 μM) measured by NBD fluorescence in 5 mM DDM at room temperature. Activity of GlpG is defined as the initial slope of the time-dependent change of fluorescence intensity. The "relative fluorescence" was obtained by taking the ratio of intensities in the presence of GlpG (without biotin labels) and LYTM2 to those in the presence of LYTM2 only.

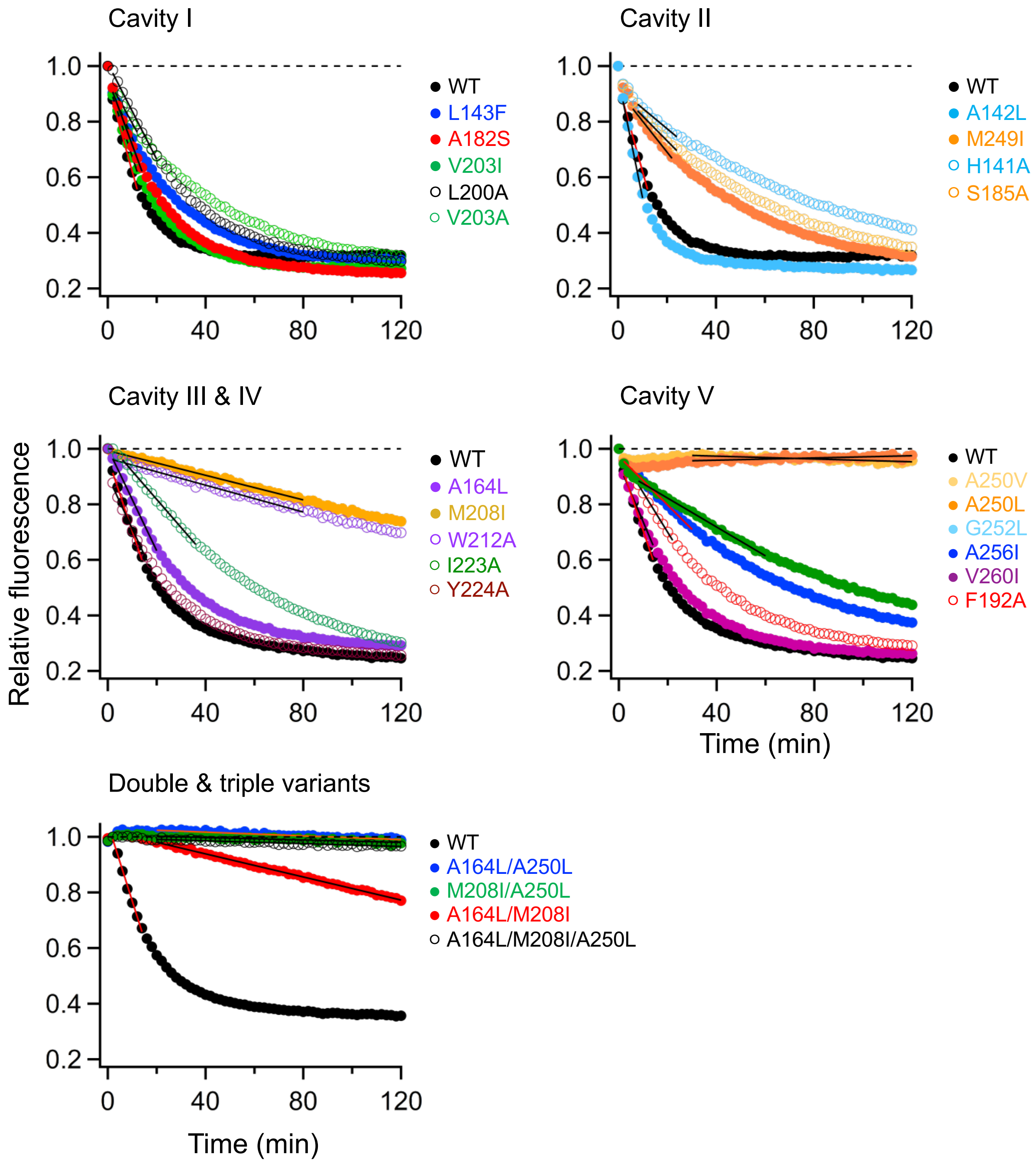

Fig. S12: Activity assay of GlpG WT and variants using the membrane-bound substrate LYTM2 in DMPC/CHAPS bicelles. Time-dependent cleavage of LYTM2 (10 μM) by GlpG variants (1 μM) measured by NBD fluorescence (**Fig. S11A**) in 1.5% (m/v) DMPC:CHAPS ([DMPC]/[CHAPS] = 2.5) bicelles at room temperature. The activity of GlpG is defined as the initial slope of the time-dependent change of fluorescence intensity.

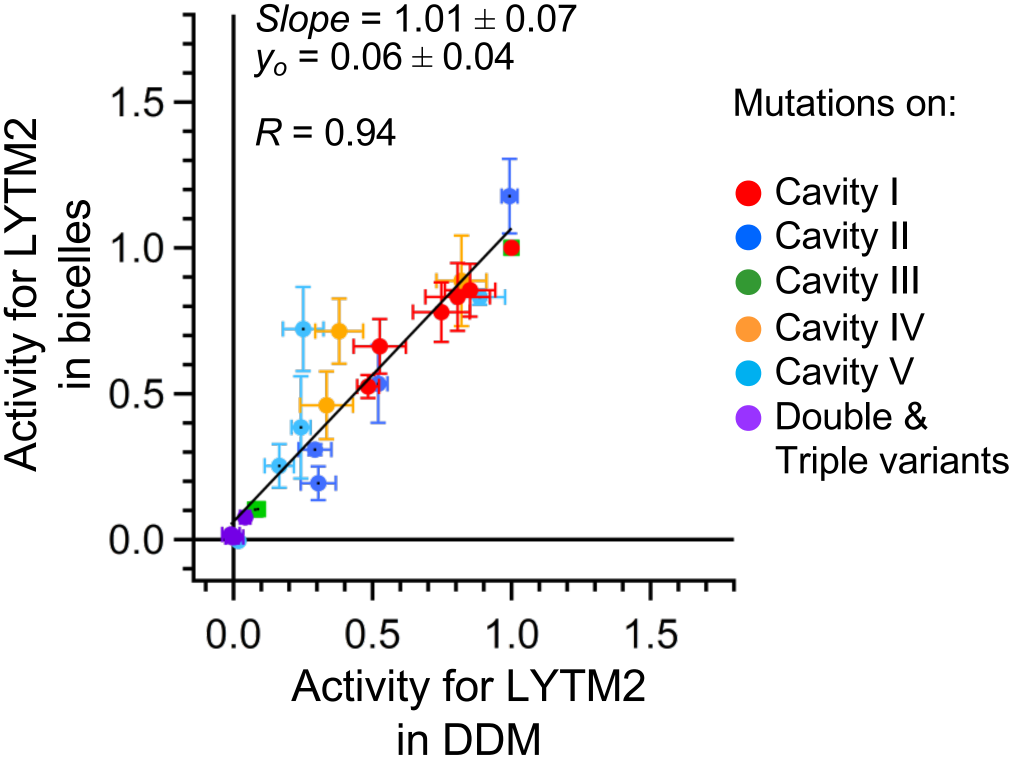

Fig. S13: Proteolytic activities of GlpG variants in micelles and bilayers. The correlation between the relative activities to WT in micelles (DDM) and bicelles (DMPC:CHAPS, molar ratio = 2.5:1) for LYTM2.

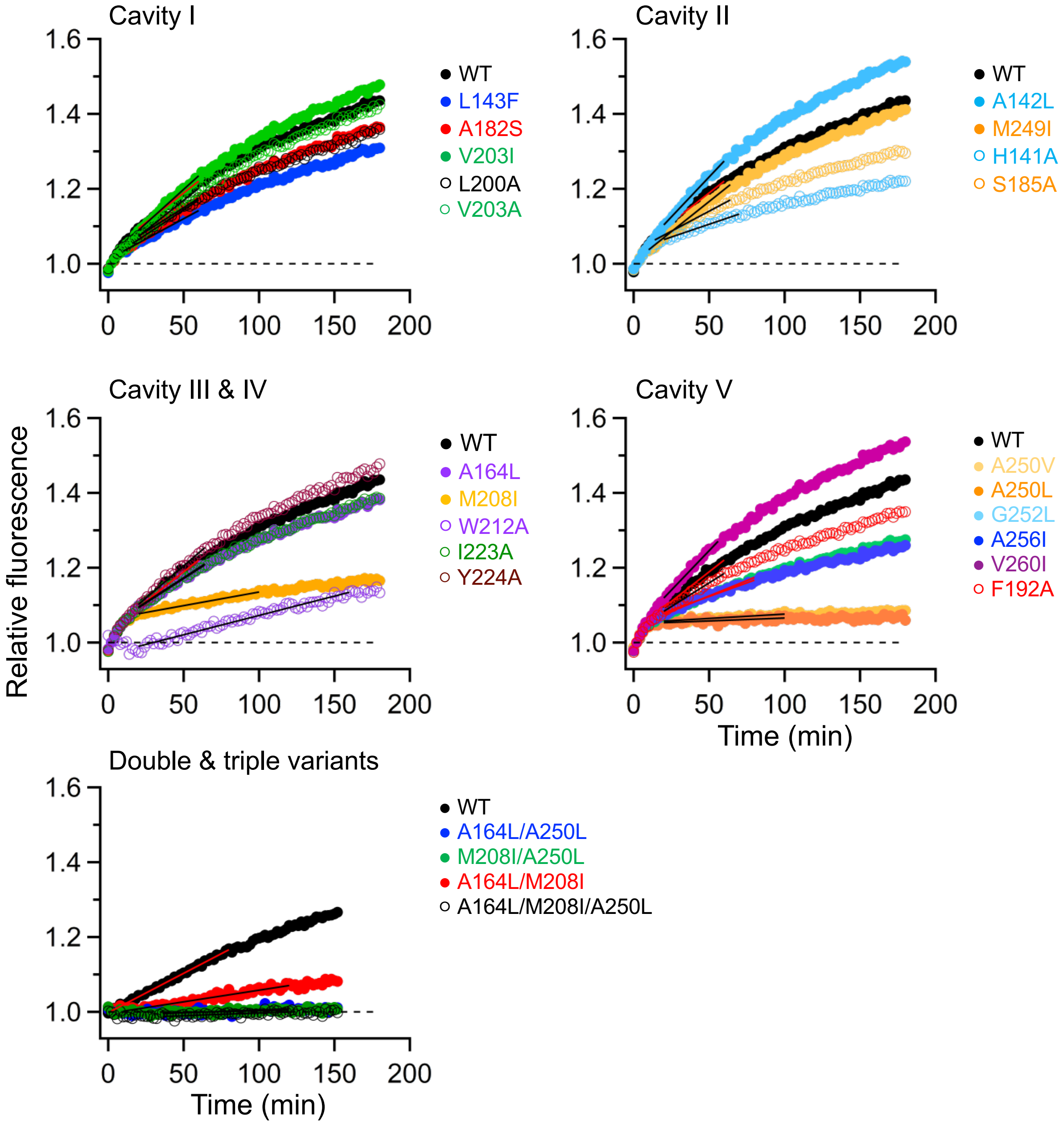

Fig. S14: Activity assay of GlpG WT and variants using water-soluble Bodipy FL-labeled casein in DDM micelles. Time-dependent cleavage of Bodipy FL-labeled casein (5 μM) by GlpG variants (5 μM) measured by Bodipy FL fluorescence in 5 mM DDM at 37°C. The activity of GlpG is defined as the initial slope of the time-dependent change of fluorescence intensity. The relative fluorescence was obtained by taking the ratio of intensities in the presence of GlpG (without biotin labels) and Bodipy FL-casein to those in the presence of Bodipy FL-casein only.

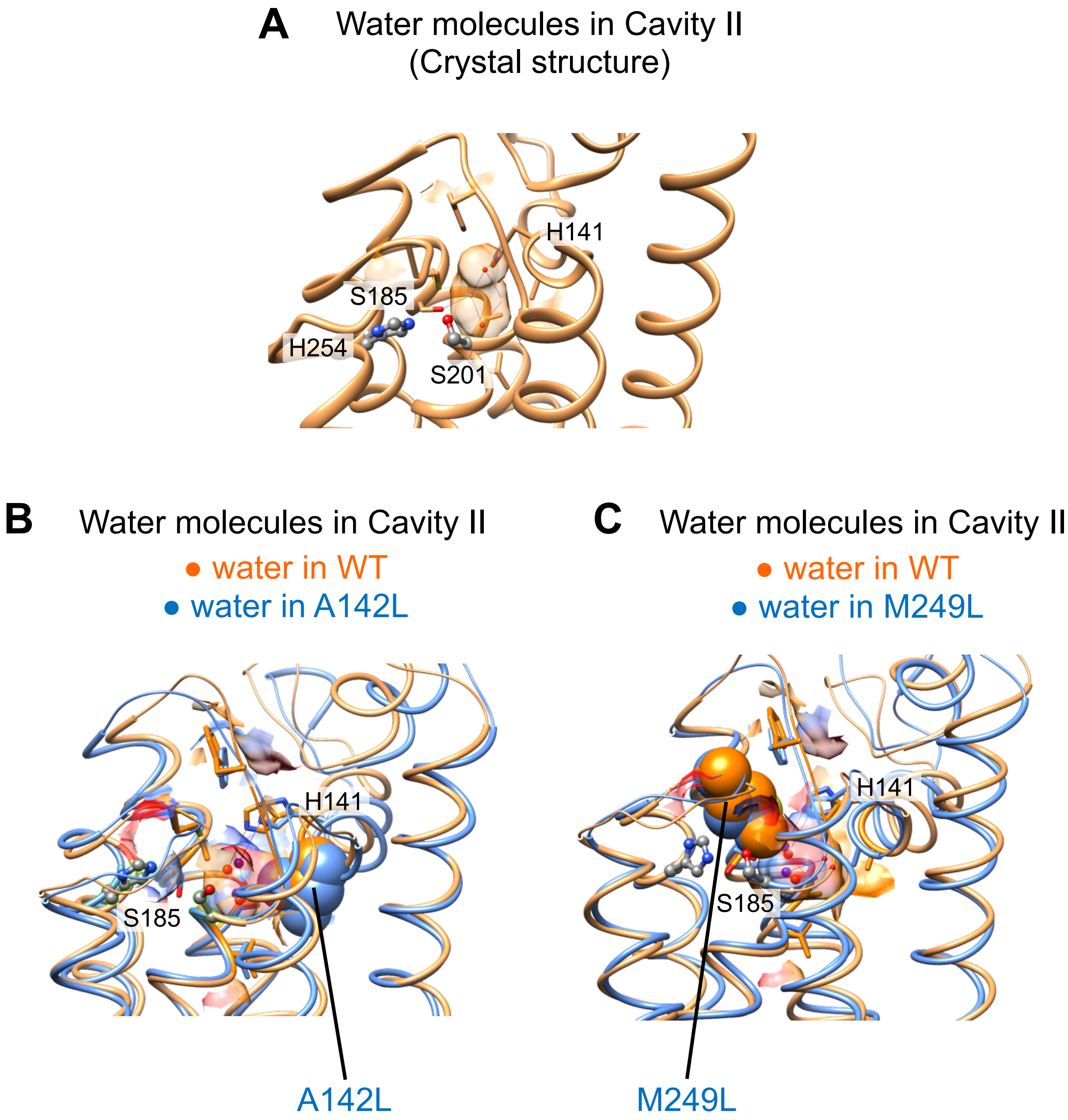

A Water molecules in Cavity II (Crystal structure)

B Water molecules in Cavity II

● water in WT

● water in A142L

C Water molecules in Cavity II

● water in WT

● water in M249L

Fig. S15: Retention of water molecules in Cavity II upon the cavity-filling mutations A142L and M249L. ***(A)*** Cavity II (water-retention site) in the crystal structure of GlpG (PDB code: 3B45). Trapped water molecules are shown in the ball representation. The residues surrounding Cavity II (in the surface representation) are shown in the stick representation. The catalytic dyad (S201-H254) is shown in the ball-and-stick representation. The hydrogen bonds mediated by the trapped water-molecules are shown in the line representation. The polar residues in the surrounding the cavity are shown with black text labels. ***(B and C)*** Comparison of the water pockets (Cavity II) in WT (orange) vs A142L (cyan in ***B***) or WT (orange) vs M249L variant (cyan in ***B***). The structures are the snapshots at 1 μs from MD simulation. In both variant structures, two water molecules are retained over the simulation as in the WT structure.

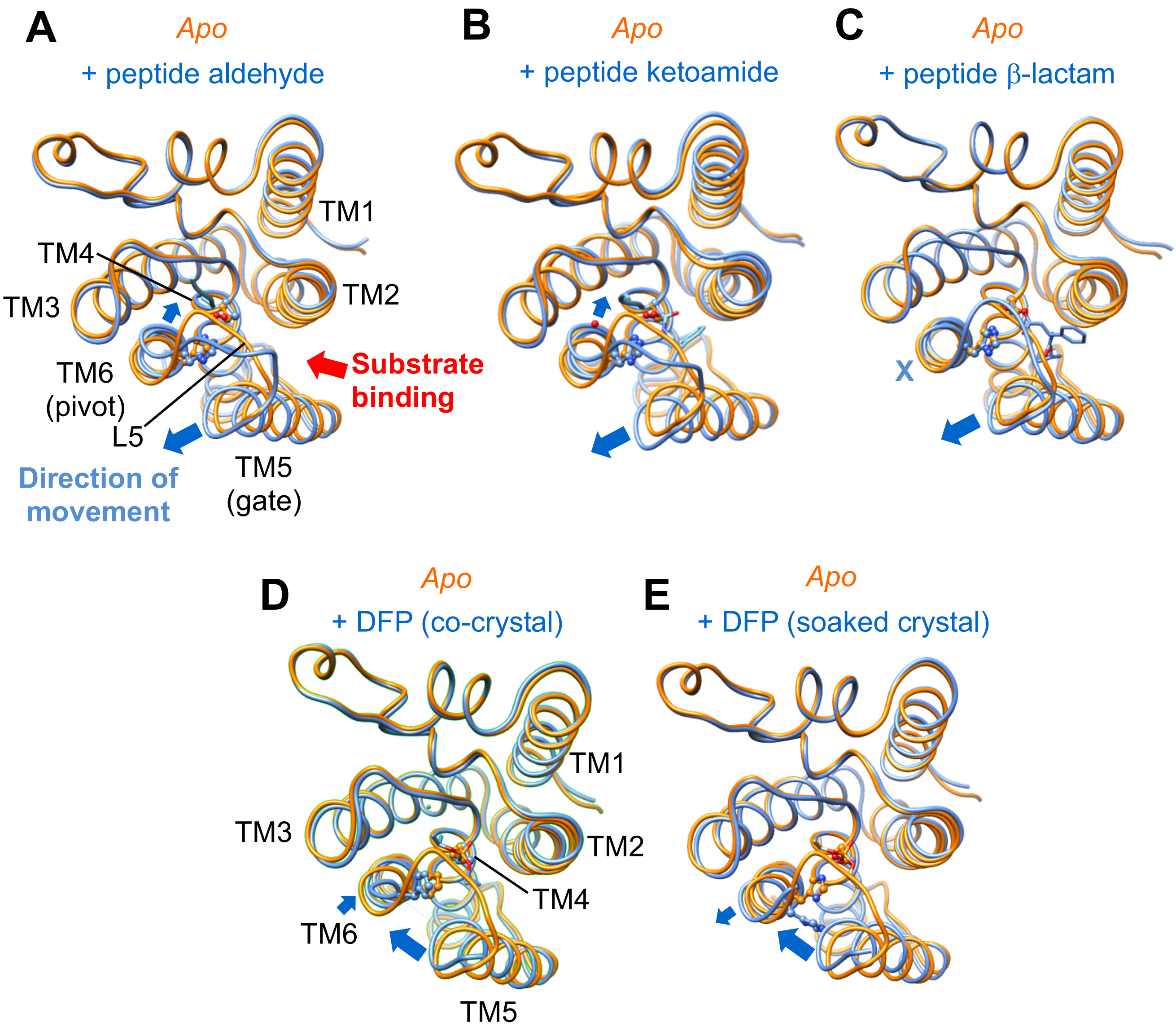

Fig. S16: Comparisons of *apo* and inhibitor-bound structures of *E. coli* GlpG indicating the movement of TM5 (gate) and TM6 (pivot). In each panel, the crystal structures of *apo* (orange, PDB code: 3B45) and an inhibitor-bound form (light blue) were superimposed using the Matchmaker tool in the UCSF Chimera program. The direction of movement of TM5 and TM6 are marked with blue arrows. No movement is marked with X.The substrate binding site is marked with a red arrow. The PDB codes of the inhibitor-bound structures used for the superposition are: ***(A)*** 5F5B (complexed with peptidic inhibitor Ac-VRMA-CHO); ***(B)*** 5MT6 (complexed with peptide derived inhibitor Ac-RVRHA-phenylethyl-ketoamide); ***(C)*** 3ZMH (complexed with monobactam L62); ***(D)*** 4H1D (complexed with DFP, *i.e.*, diisopropyl fluorophosphate, co-crystal); ***(E)*** 3TXT (complexed with DFP, diisopropyl fluorophosphate, soaked crystal). The side chains of the catalytic dyad (Ser201 on TM4 and His254 on TM6, ball- and-stick representation) and the inhibitors (stick representation) covalently attached to Ser201 are also shown.

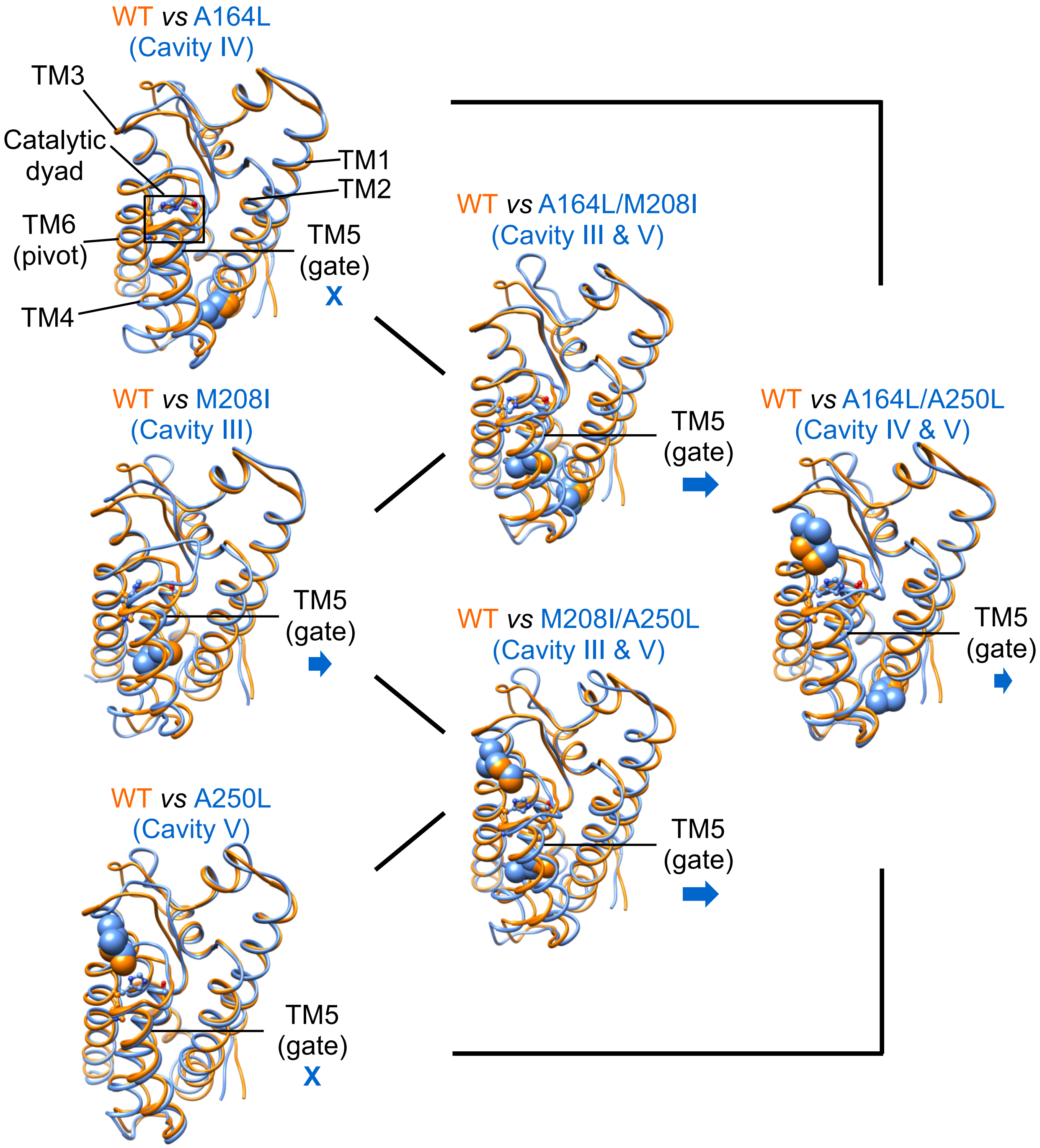

Fig. S17: The impact of the cavity-filling and inactivating mutations on the conformation of GlpG. The conformational changes of *E. coli* GlpG induced by the cavity-filling and inactivating mutations observed in MD simulation. In each panel, the structural snapshots of WT (orange) and a cavity-filled variant (light blue) at 1 μs in the simulation are superimposed. For the single (left column) and double (central column) variants involving M208I mutation on Cavity III, the most noticeable conformational changes are the gate-closing movement of TM5 (blue arrows, see also **Fig. S18**). The variant with no noticeable movement of TM5 is marked with X. The amplitude of this movement is negligible for A164L on Cavity IV and A250L on Cavity V. The side chains of the active site residues (Ser201 and His254) are shown in the ball-and-stick model, and the residues of WT and variants at the mutation sites are shown in the sphere model.

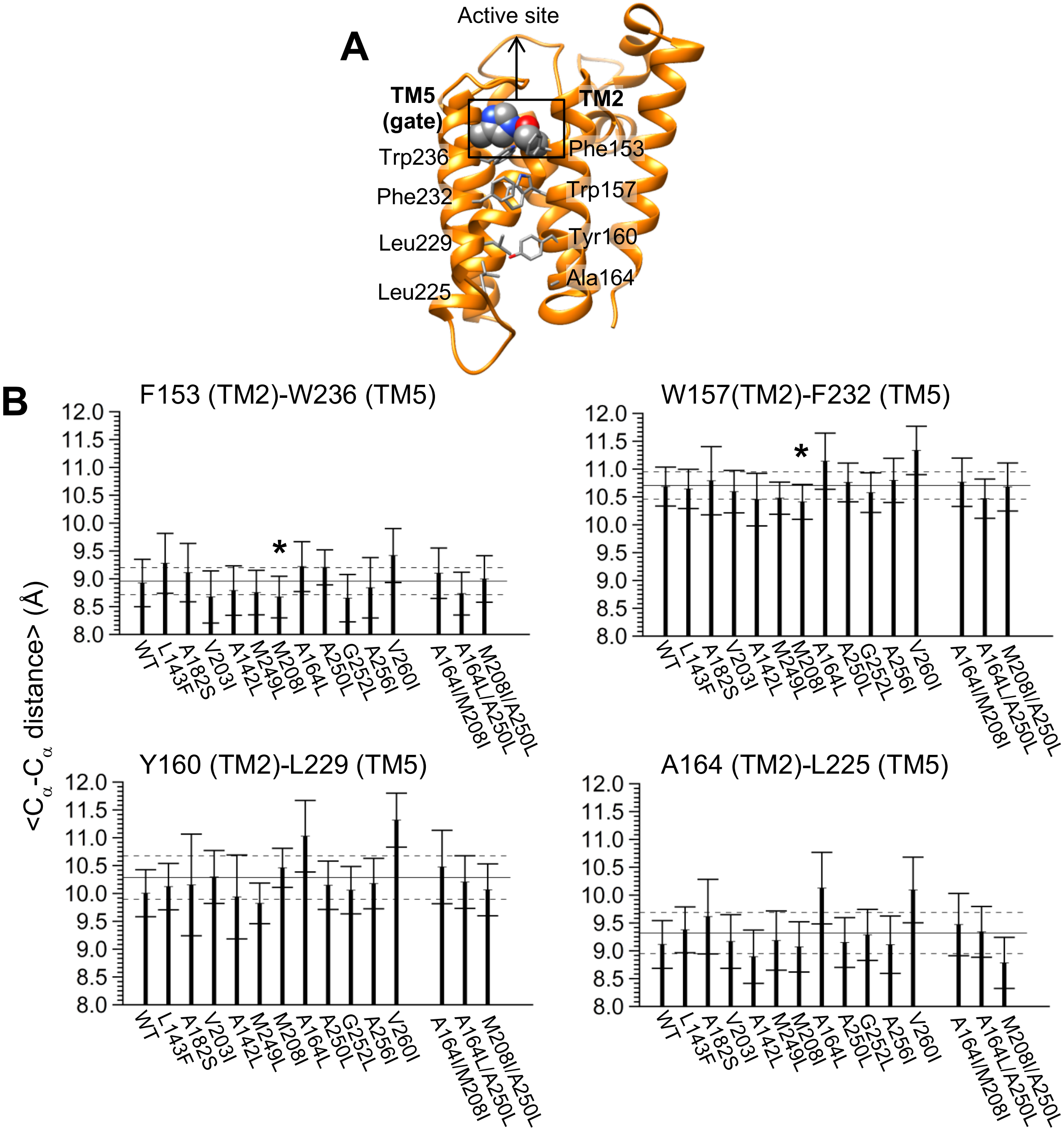

Fig. S18: The effects of cavity-filling mutations on the substrate binding site. ***(A)*** The structure of the substrate binding site (the TM2-TM5 interface). ***(B)*** For WT and each variant, the inter-residue distances ($d_{C\alpha\text{-}C\alpha}$) between the gating helix TM5 and TM2 were averaged over all time frames in MD simulation $<d_{C\alpha\text{-}C\alpha}>$. Error bars designate the standard deviations of fluctuating $d_{C\alpha\text{-}C\alpha}$. In each plot, the solid horizontal lines indicate the average of the $<d_{C\alpha\text{-}C\alpha}>$ values over WT and all variants ($<<d_{C\alpha\text{-}C\alpha}>>_{WT,variants}$). The dashed horizontal lines denote the standard deviation of the $<d_{C\alpha\text{-}C\alpha}>$ values ($<<d_{C\alpha\text{-}C\alpha}>> \pm \sigma_{dC\alpha\text{-}C\alpha}$). The cavity-filling mutations that reduce each interatomic distance lower than $<<d_{C\alpha\text{-}C\alpha}>> - \sigma_{dC\alpha\text{-}C\alpha}$ are regarded as shrinking the gate and marked with asterisks.

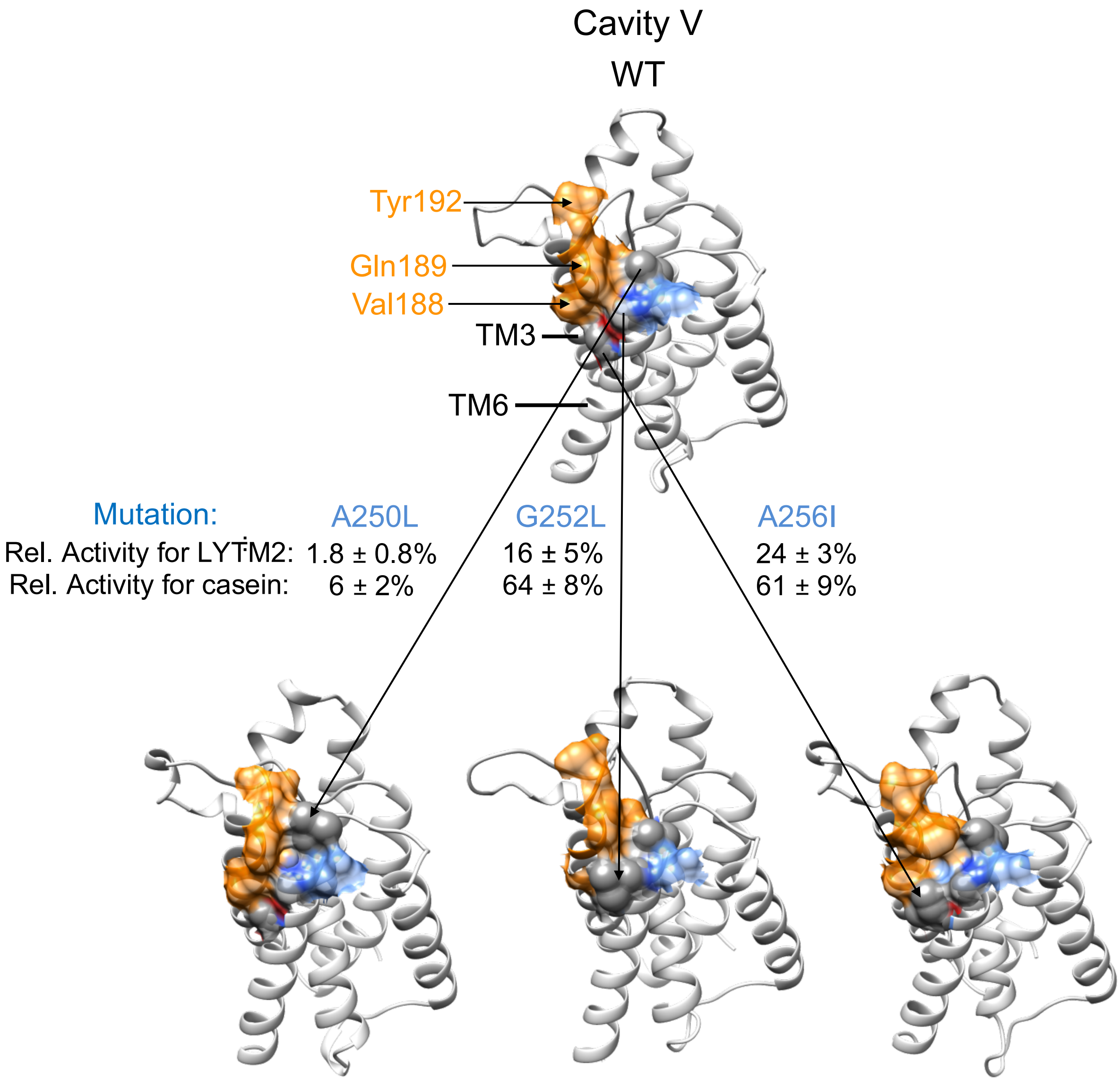

Mutation:	A250L	G252L	A256I
Rel. Activity for LYTM2:	1.8 ± 0.8%	16 ± 5%	24 ± 3%
Rel. Activity for casein:	6 ± 2%	64 ± 8%	61 ± 9%

Fig. S19: The effects of cavity-filling mutations on Cavity V. (*Top*) Cavity V is formed by the residues at the interface between TM3 (orange) and TM6 (blue) in the periplasmic side. **(*Bottom*)** The small-to-large mutations on TM6 (the substituted residues are shown in the sphere model in grey) are expected to inhibit the pivot movement of the top half of TM6 (**Fig. S16**) leading to the activity loss. The activities of the variants for the membrane-bound substrate LYTM2 and for the water-soluble substrate casein are shown.

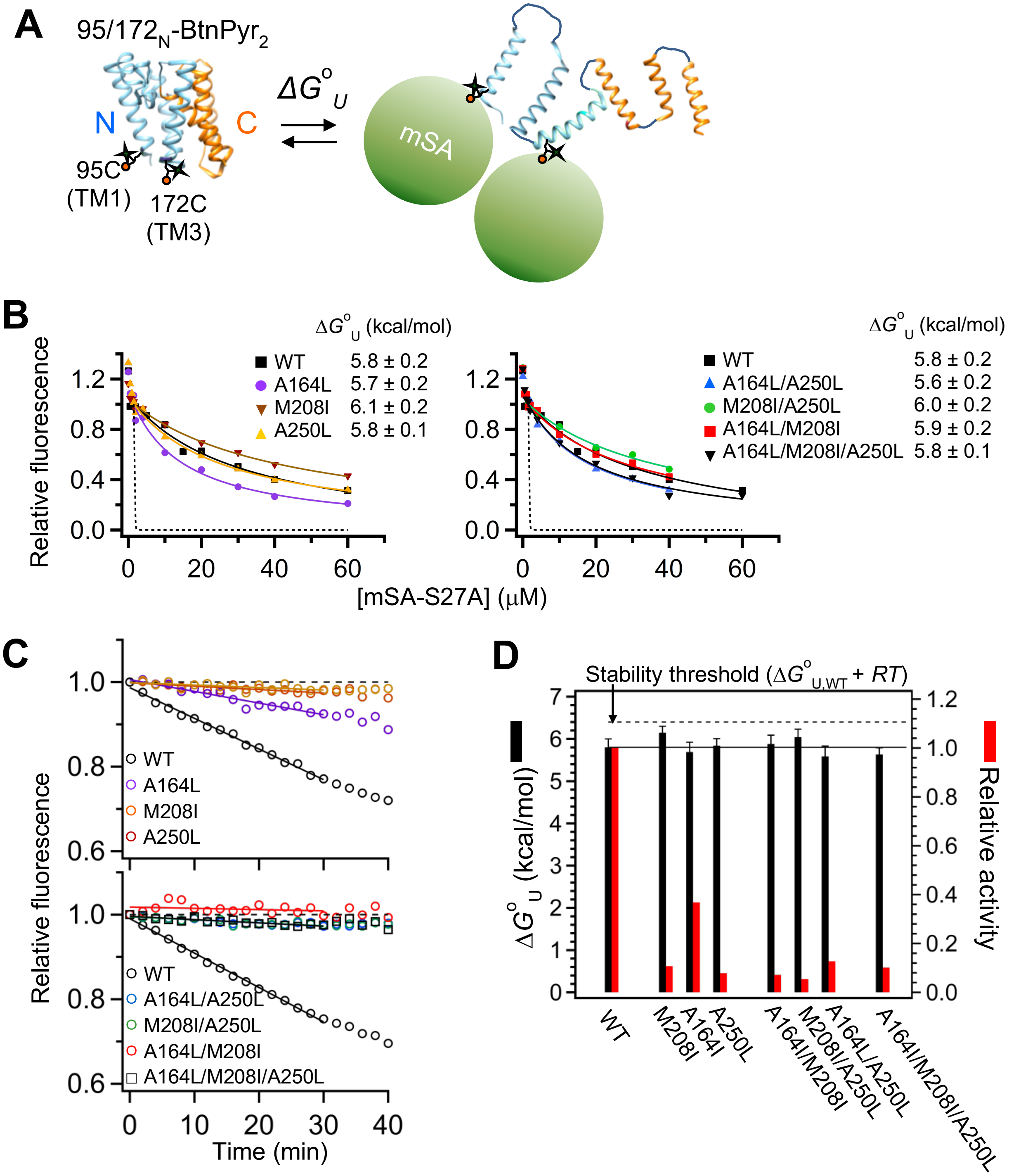

Fig. S20: The impact of cavity-filling mutations on the stability and activity of GlpG measured at an N-terminal biotin pair. ***(A)*** The location of the biotin pair 95/172-BtnPyr$_2$ for measuring Δ*G*°$_U$ of GlpG at the N-subdomain. ***(B–D)*** The stability and activity of GlpG WT and the variants with the stabilizing cavity-filling mutations. ***(B)*** Δ*G*°$_U$'s were measured using steric trapping (dashed line in each plot: intrinsic binding), and ***(C)*** the activities were measured using NBD-labeled LYTM2 in 5 mM DDM. ***(D)*** The fitted Δ*G*°$_U$'s and activities are summarized.

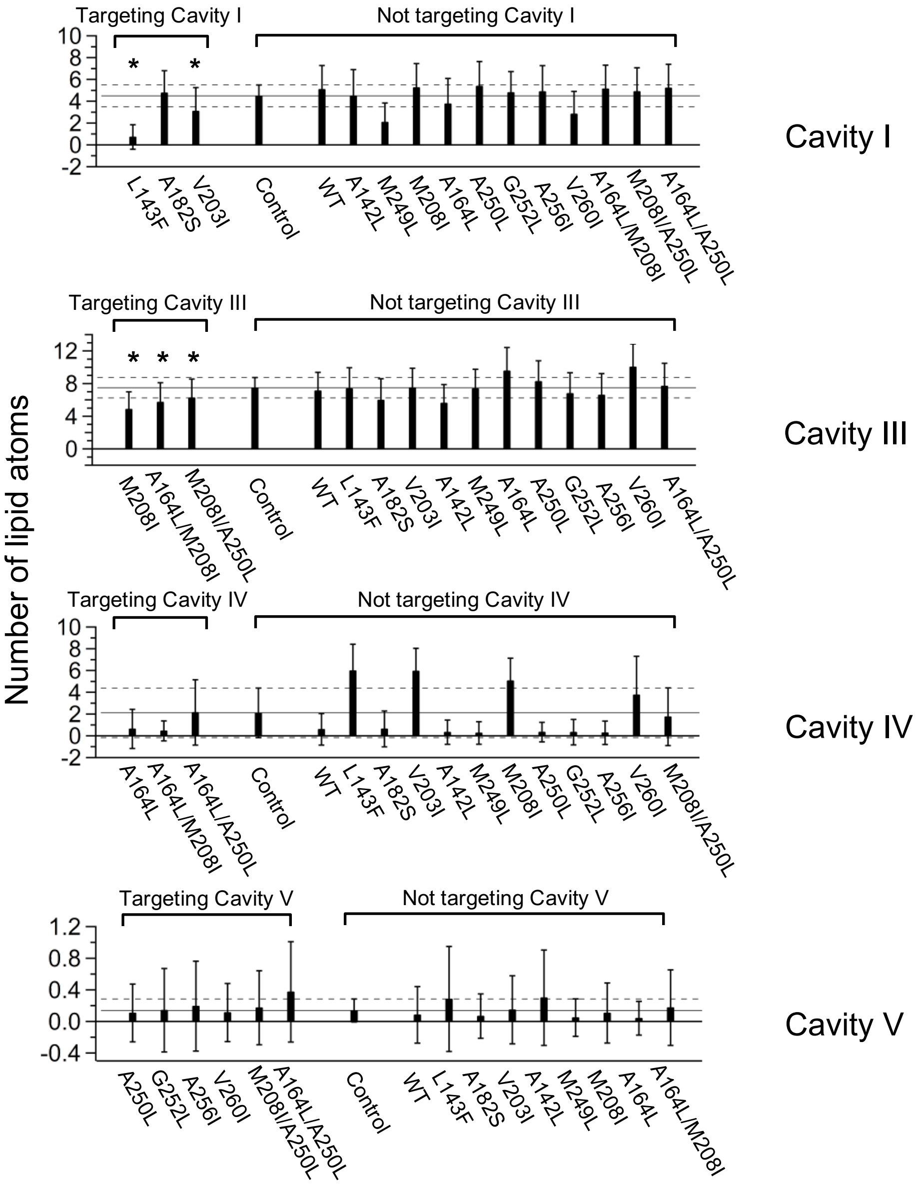

Fig. S21: The influence of cavity-filling mutations on the lipid occupancy of the cavities. For all variants, the number of lipid heavy atoms, whose centers of mass reside within the void volume of each designated cavity, were counted and averaged over all time frames in MD simulation ($<N_{\mathrm{Lipid,cavity}}>$). Each error bar represents the standard deviation of the fluctuation in $N_{\mathrm{Lipid,cavity}}$. “Control” indicates the average of the $<N_{\mathrm{Lipid,cavity}}>$ values for a designated cavity in WT and the variants that do not contain a mutation in that cavity (*i.e.*, $<<N_{\mathrm{Lipid,cavity}}>>_{\text{not-targeted}}$, solid horizontal lines). The dashed horizontal lines denote the standard deviation of the $<N_{\mathrm{Lipid,cavity}}>$ values ($<<N_{\mathrm{Lipid,cavity}}>>_{\text{not-targeted}} \pm \sigma_{<N\_\mathrm{Lipid,cavity}>\text{not-targeted}}$). The cavity-filling mutations that reduce the $<N_{\mathrm{Lipid,cavity}}>$ value lower than $<<N_{\mathrm{Lipid,cavity}}>>_{\text{not-targeted}} - \sigma_{<N\_\mathrm{Lipid,cavity}>\text{not-targeted}}$ are regarded as significantly displacing the solvated lipid atoms and marked with asterisks.

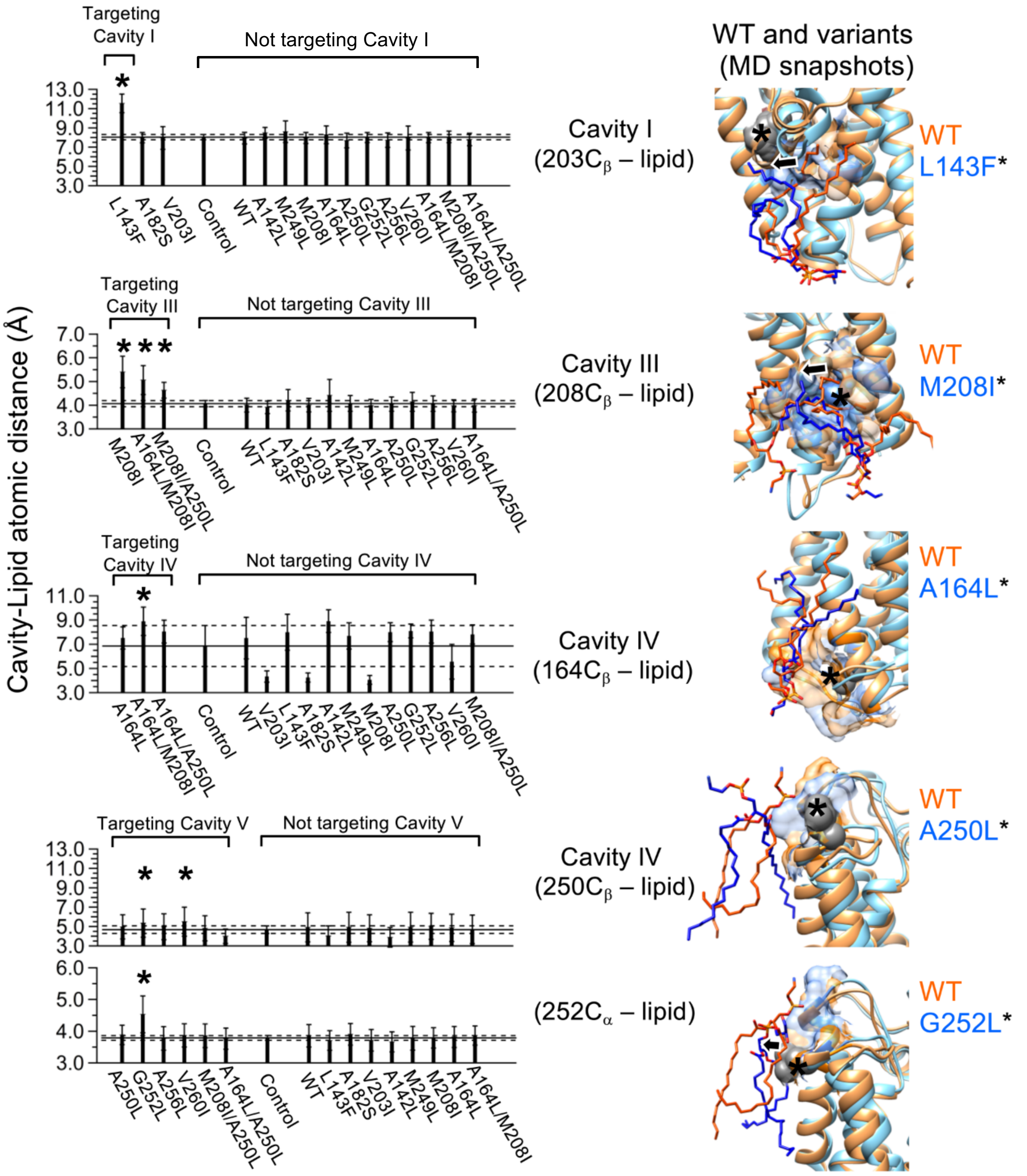

Fig. S22: The influence of cavity-filling mutations on the cavity-lipid distances.
(*Left*) The interatomic distances between the designated residue atom in each cavity and the closest approaching lipid heavy atom. Each value was measured and averaged over all time frames in MD simulation ($\langle d_{\text{Cavity-lipid}} \rangle$). Each error bar represents the standard deviation of the fluctuation in $d_{\text{Cavity-lipid}}$. “Control” indicates the average of the $\langle d_{\text{Cavity-lipid}} \rangle$ values for a specific cavity in WT and the variants that do not contain a mutation in that cavity (*i.e.*, $\langle\langle d_{\text{Cavity-lipid}} \rangle\rangle_{\text{not-targeted}}$, solid horizontal lines). The dashed horizontal lines denote the standard deviation of the $\langle d_{\text{Cavity-lipid}} \rangle$ values ($\langle\langle d_{\text{Cavity-lipid}} \rangle\rangle_{\text{not-targeted}} \pm \sigma_{\langle d\_\text{Cavity-lipid} \rangle \text{not-targeted}}$). The cavity-filling mutations that increase the $\langle d_{\text{Cavity-lipid}} \rangle$ value lower than $\langle\langle d_{\text{Cavity-lipid}} \rangle\rangle_{\text{not-targeted}} \pm \sigma_{\langle d\_\text{Cavity-lipid} \rangle \text{not-targeted}}$ are regarded as displacing the solvated lipid atoms and marked with asterisks.
(*Right*) MD snapshots of lipid-protein interactions. In each figure, WT (orange) and a cavity-filled variant (blue) were compared. The asterisk marks designate the position of mutation. The black arrows indicate noticeable movements of the lipid segment near the cavity induced by mutation.

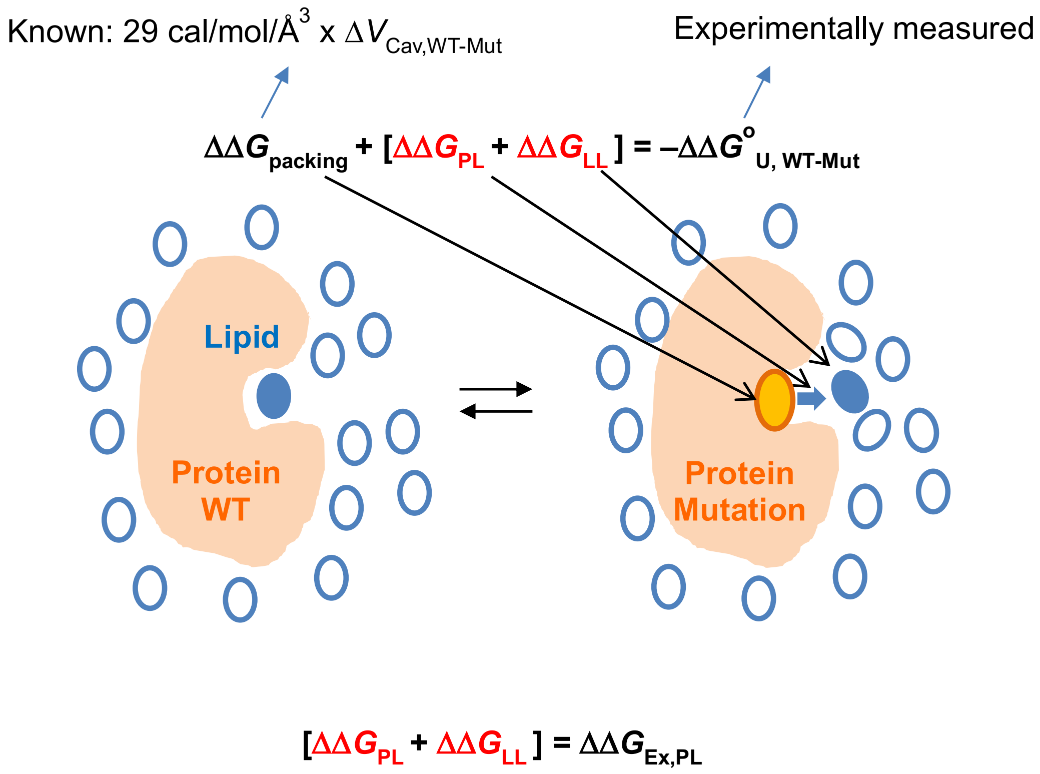

Fig. S23: Scheme of the "perturbation" approach for quantifying the lipid solvation energy using the packing-desolvation coupling. Our MD simulation study indicates that the cavity-filling mutation (*i.e.*, the improvement of packing, $\Delta\Delta G_{\mathrm{packing}}$) is coupled to the displacement or additional binding of lipid molecules in the cavity targeted for mutation ($\Delta\Delta G_{\mathrm{PL}} + \Delta\Delta G_{\mathrm{LL}}$). The energetic contributions involving the protein-lipid interaction and the associated changes in lipid-lipid interaction ($\Delta\Delta G_{\mathrm{PL}} + \Delta\Delta G_{\mathrm{LL}}$) can define the lipid exchange term, $\Delta\Delta G_{\mathrm{Ex,PL}}$, which represents the net preference of lipid binding on the cavity relative to the interaction with the bulk lipid phase. The stability change of GlpG ($-\Delta\Delta G^{\mathrm{o}}_{\mathrm{U,WT\text{-}Mut}}$) can be described as the net outcome of two energetic contributions $\Delta\Delta G_{\mathrm{packing}} + \Delta\Delta G_{\mathrm{Ex,PL}}$ (**Eq. 2** in the main text). The packing contribution to protein stability ($\Delta\Delta G_{\mathrm{packing}} = -30$ to -24 cal/mol/Å^3) has been measured previously by the Matthews and Bowie groups independently (20, 21). The change in the cavity volume upon mutation ($\Delta V_{\mathrm{Cav,WT\text{-}Mut}}$) can be obtained from MD simulation (**Fig. S6**). $\Delta\Delta G^{\mathrm{o}}_{\mathrm{U,WT\text{-}Mut}}$ can be measured using steric trapping (**Fig. 2** and **Fig. S10**).

Table S1. List of cavities (voids and pockets) in *E. coli* GlpG identified on the CASTp server (http://sts.bioe.uic.edu/castp/) using the probe radius of 1.4 Å. The area and volume were computed on the molecular surface of each cavity.

Cavity ID from CASTp	Area (Å^2)	Volume (Å^3)	Cavity ID from this study
1	118.237	141.676	Cavity III
2	127.691	150.6	Cavity IV
3	75.831	75.817	
4	23.502	30.178	
5	84.111	55.615	Cavity I
6	23.367	22.337	
7	106.6	82.963	Cavity II
8	59.469	47.28	Cavity V
9	1.701	3.862	
10	26.503	17.464	
11	16.545	11.181	
12	26.404	16.067	
13	1.928	1.989	
14	37.51	20.431	
15	39.751	21.496	
16	38.255	16.155	
17	42.874	17.331	
18	30.012	15.225	
19	19.778	8.33	
20	29.572	14.613	
21	27.025	13.189	
22	26.376	12.708	
23	25.574	11.868	
24	14.992	6.692	

Table S2. The list of heavy atoms in the residues contacting the five major cavities targeted in this study. The cavity atoms were obtained from the CASTp server using the *E. coli* GlpG structure (PDB code: 3B45). Number: residue number; @: atomic identifier.

Cavity ID from this study	Heavy atoms in the residues contacting the cavity	Fraction of electronegative atoms (N and O)
Cavity I	100@Cε; 139@O, Cβ, Cδ2; 142@Cδ; 178@Cγ2; 179@Cα, Cδ2; 182@Cδ; 200@Cδ2; 203@Cγ2	0.09
Cavity II	141@Nδ1, Cε1; 142@Cβ; 182@Cα; 185@Oγ; 197@Cδ1, Cε1; 198@Cα, C; 199@O; 202@N, Cα; 203@N, Cγ2; 249@Sδ, Cε	0.31
Cavity III	208@C, O, Cβ, Sδ; 209@N; 212@Cβ, Cγ, Cδ1, Cδ2, Nε1, Cε2, Cε3; 225@Cδ2; 230@O, Cγ2, Cβ; 234@Cγ, Cδ2; 237@Cδ1; 258@Cδ1; 262@Cδ2	0.19
Cavity IV	160@Cε1,Cε2,Cζ, OH; 161@Cα, Cδ2; 164@Cβ; 168@Cδ, Nε, Cζ, NH2; 211@Cγ; 222@O; 223@Cα, Cγ1; 224@N, O, Cδ2, Cε1, Cε2, Cζ, OH	0.32
Cavity V	188@O, Cγ1; 189@Cα, Oε1; 192@Cβ, Cδ1; 193@Oγ; 250@Cβ; 252@Cα; 253@N, Cβ	0.36

Table S3: Volumes for Cavity I_{bR} and Cavity $\mathrm{II}_{\mathrm{bR}}$ evaluated from MD simulation

		MD Simulation				Experiment[a]	
	Protein	V_{I} ($Å^3$)	σ_{I} ($Å^3$)[b]	V_{II} ($Å^3$)[b]	σ_{II} ($Å^3$)	ΔV_{Exp} ($Å^3$)[c]	$\Delta\Delta G^{o}_{\mathrm{U,WT\text{-}Mut}}$[e] (kcal/mol)
	WT	4.2	5.0	30.4	17.1	-	0
Group 1	L94A	35.4	29.2	20.4	13.3	93	-3.1
	L111A	5.6	7.5	90.5	29.0	58[d]	-1.7
	I148A	39.1	23.7	134.2	25.1	90[d]	-2.3
	I148V	7.8	6.6	35.1	21.1	30[d]	-0.9
	L152A	14.3	15.7	21.6	13.7	50	-1.7
Group 2	V49A	7.7	7.5	89.3	33.3	14	-0.5

[a] Experimental data obtained from Joh *et al. JACS* **2009** 131, 10846-10847 (20).

[b] Standard deviation.

[c] Cavity volumes were measured for the cavity next to a given site of mutation using the grid-based method (30).

[d] Weighted average of multiple side-chain conformations (20).

Table S4: Fitted parameters to the linear-response model for predicting the stability changes ($\Delta\Delta G^{o}_{U,WT\text{-}Mut,Simul}$) upon mutation on the basis of the volume changes obtained from MD simulation. In the linear-response model, $\Delta\Delta G^{o}_{U,WT\text{-}Mut,Sim} = c_{I}\Delta V_{I,WT\text{-}Mut} + c_{II}\Delta V_{II,WT\text{-}Mut} + b$ (**Eq. S1** in ***SI Appendix*** or **Eq. 1** in the main text), $\Delta V_{I,WT\text{-}Mut}$ and $\Delta V_{II,WT\text{-}Mut}$ indicate the mutation-induced volume changes of Cavity $\mathbf{I}_{bR}$ and Cavity $\mathbf{II}_{bR}$ relative to those in WT, respectively. The coefficients c_{I} and c_{II} represent the packing contribution to the stability in the two corresponding cavities, and the constant b is related to the lipid or water solvation contribution upon mutation. The coefficients c_{I}, c_{II} and b are simultaneously determined by the model fitting.

	c_{I} (kcal/mol/Å^3)	c_{II} (kcal/mol/Å^3)	b (kcal/mol)	R
All variants	–0.05 ± 0.02	0.01 ± 0.01	–1.12 ± 0.40	0.87
without L111A	–0.07 ± 0.01	0.01 ± 0.01	–0.79 ± 0.01	0.99_5

Table S5: The influence of cavity-filling mutations on the hydrogen bond in the catalytic dyad (Ser201$_{O\gamma}$–His254$_{N\varepsilon2}$). For each variant, the fluctuating interatomic distances between Ser201 and His254 were averaged over the MD frames, from which the standard deviations were calculated.

GlpG variant	**Average distance (Å) Ser201$_{O\gamma}$–His254$_{N\varepsilon2}$**	**Standard deviation (Å)**
WT	2.885	0.156
V203I	2.871	0.130
L143F	2.882	0.142
A182S	2.842	0.120
A142L	2.860	0.126
M249L	2.882	0.137
M208I	2.914	0.151
A164L	2.898	0.154
A250L	2.862	0.126
G252L	2.851	0.123
A256I	2.896	0.157
V260I	2.892	0.179
A164L/M208I	2.881	0.139
A164L/A250L	2.844	0.121
M208I/A250L	2.881	0.162

SI References

1. M. K. Lemberg, M. Freeman, Functional and evolutionary implications of enhanced genomic analysis of rhomboid intramembrane proteases. *Genome Res* **17**, 1634-1646 (2007).
2. A. Leaver-Fay *et al.*, ROSETTA3: an object-oriented software suite for the simulation and design of macromolecules. *Methods Enzymol* **487**, 545-574 (2011).
3. Y. Wang, Y. Zhang, Y. Ha, Crystal structure of a rhomboid family intramembrane protease. *Nature* **444**, 179-180 (2006).
4. K. R. Vinothkumar *et al.*, The structural basis for catalysis and substrate specificity of a rhomboid protease. *EMBO J* **29**, 3797-3809 (2010).
5. Y. Wang, S. Maegawa, Y. Akiyama, Y. Ha, The role of L1 loop in the mechanism of rhomboid intramembrane protease GlpG. *J Mol Biol* **374**, 1104-1113 (2007).
6. D. E. Kim, D. Chivian, D. Baker, Protein structure prediction and analysis using the Robetta server. *Nucleic Acids Res* **32**, W526-531 (2004).
7. W. Humphrey, A. Dalke, K. Schulten, VMD: visual molecular dynamics. *J Mol Graph* **14**, 33-38, 27-38 (1996).
8. J. C. Phillips *et al.*, Scalable molecular dynamics with NAMD. *J Comput Chem* **26**, 1781-1802 (2005).
9. A. Aksimentiev, M. Sotomayor, D. Wells, Membrane Proteins Tutorial. *University of Illinois at Urbana Champaign* (2012).
10. B. R. Brooks *et al.*, CHARMM: the biomolecular simulation program. *J Comput Chem* **30**, 1545-1614 (2009).
11. M. J. Lemieux, S. J. Fischer, M. M. Cherney, K. S. Bateman, M. N. James, The crystal structure of the rhomboid peptidase from *Haemophilus influenzae* provides insight into intramembrane proteolysis. *Proc Natl Acad Sci U S A* **104**, 750-754 (2007).
12. E. F. Pettersen *et al.*, UCSF Chimera--a visualization system for exploratory research and analysis. *J Comput Chem* **25**, 1605-1612 (2004).
13. J. Dundas *et al.*, CASTp: computed atlas of surface topography of proteins with structural and topographical mapping of functionally annotated residues. *Nucleic Acids Res* **34**, W116-118 (2006).
14. S. Jo, T. Kim, V. G. Iyer, W. Im, CHARMM-GUI: a web-based graphical user interface for CHARMM. *J Comput Chem* **29**, 1859-1865 (2008).
15. W. L. Jorgensen, J. Chandrasekhar, J. D. Madura, R. W. Impey, M. L. Klein, COMPARISON OF SIMPLE POTENTIAL FUNCTIONS FOR SIMULATING LIQUID WATER. *Journal of Chemical Physics* **79**, 926-935 (1983).
16. R. B. Best *et al.*, Optimization of the additive CHARMM all-atom protein force field targeting improved sampling of the backbone phi, psi and side-chain chi(1) and chi(2) dihedral angles. *J Chem Theory Comput* **8**, 3257-3273 (2012).
17. T. Darden, D. York, L. Pedersen, PARTICLE MESH EWALD - AN N.LOG(N) METHOD FOR EWALD SUMS IN LARGE SYSTEMS. *Journal of Chemical Physics* **98**, 10089-10092 (1993).
18. J. C. Phillips *et al.*, Scalable molecular dynamics with NAMD. *Journal of Computational Chemistry* **26**, 1781-1802 (2005).
19. T. Paramo, A. East, D. Garzon, M. B. Ulmschneider, P. J. Bond, Efficient Characterization of Protein Cavities within Molecular Simulation Trajectories: trj_cavity. *Journal of Chemical Theory and Computation* **10**, 2151-2164 (2014).
20. N. H. Joh, A. Oberai, D. Yang, J. P. Whitelegge, J. U. Bowie, Similar energetic contributions of packing in the core of membrane and water-soluble proteins. *J Am Chem Soc* **131**, 10846-10847 (2009).
21. A. E. Eriksson *et al.*, Response of a protein-structure to cavity-creating mutations and its relation to the hydrophobic effect. *Science* **255**, 178-183 (1992).
22. R. Guo *et al.*, Steric trapping reveals a cooperativity network in the intramembrane protease GlpG. *Nat Chem Biol* **12**, 353-360 (2016).
23. M. Howarth *et al.*, A monovalent streptavidin with a single femtomolar biotin binding site. *Nature methods* **3**, 267-273 (2006).
24. H. Hong, Y. C. Chang, J. U. Bowie, Measuring transmembrane helix interaction strengths in lipid bilayers using steric trapping. *Methods Mol Biol* **1063**, 37-56 (2013).
25. Y. Akiyama, S. Maegawa, Sequence features of substrates required for cleavage by GlpG, an Escherichia coli rhomboid protease. *Molecular microbiology* **64**, 1028-1037 (2007).
26. H. Hong, T. M. Blois, Z. Cao, J. U. Bowie, Method to measure strong protein-protein interactions in lipid bilayers using a steric trap. *Proc Natl Acad Sci U S A* **107**, 19802-19807 (2010).
27. T. M. Blois, H. Hong, T. H. Kim, J. U. Bowie, Protein unfolding with a steric trap. *J Am Chem Soc* **131**, 13914-13915 (2009).

28. A. Horovitz, Double-mutant cycles: A powerful tool for analyzing protein structure and function. *Fold Des* **1**, R121-R126 (1996).
29. N. Pattabiraman, K. B. Ward, P. J. Fleming, Occluded molecular surface: analysis of protein packing. *J Mol Recognit* **8**, 334-344 (1995).
30. T. Paramo, A. East, D. Garzon, M. B. Ulmschneider, P. J. Bond, Efficient Characterization of Protein Cavities within Molecular Simulation Trajectories: trj_cavity. *J Chem Theory Comput* **10**, 2151-2164 (2014).